DESIGN AND FABRICATION OF AN AUTOMATED SOIL-WATER MICRO-SAMPLING SYSTEM

by

Daniel David Collins

A thesis submitted in partial fulfillment
of the requirements for the degree

of

Master of Science

in

Mechanical Engineering

MONTANA STATE UNIVERSITY
Bozeman, Montana

May 2023

ACKNOWLEDGEMENTS

Pursuing a master's degree is no small task. Sacrifices must be made, and the nights are long. I could not have done it without the support of my wife Annika, thank you. I would like to thank my committee chair Stephan Warnat and the other committee members Craig Shankwitz and Rob Payn for helping me grow tremendously as a scientist and engineer. My colleges in the Warnat lab group and the Signals in the Soil team have helped me greatly to understand the fundamentals of 3D printing, microfabrication, analysis, and experimentation; for that I am extremely thankful. I would also like to take this opportunity to thank the National Science Foundation for providing the financial support for the Signals in the Soil project, NSF award number 2034430. The COMSOL work was performed in part at the Montana Nanotechnology Facility, an NNCI member supported by NSF Grant ECCS-2025391.

TABLE OF CONTENTS

1. INTRODUCTION 1

Background & Motivation 1
Research Goals & Objectives 5
A Review of Current Automated Water Analysis Systems 6
Soil Nutrient Management and Drinking Water Quality 6
An Evaluation of Existing Microsensor Technologies for Environmental Monitoring 12
Optical Transducers 12
Absorbance 13
Colorimetry 13
Electrochemical Transducers 14
Ion Selective Electrodes 14
Voltammetry 15
Electrochemical Impedance Spectroscopy (EIS) 16
Summary 18
Fundamentals of EIS 18

2. MATERIALS & METHODOLOGY 22

MESA System: Description 22
Smart-Reservoir Module 26
Multifunctional Sensor Module 28
Cleaning Solution Module 32
MESA System: Assembly 33
MESA System: Testing Procedures 33
Calibration 33
Packaging Experiment 34
Cleaning Cycle Experiment 34
Emulated Field Experiment 36

3. RESULTS & DISCUSSIONS 33

Electrical Conductivity Sensor 39
Best Analysis Frequency Determination 39
Calibration 41
Packaging Considerations 45
Transient Cleaning Cycle Analysis 47
Emulated Field Experiment 52

4. CONCLUSIONS & FUTURE OUTLOOK 55

REFERENCES CITED 57

TABLE OF CONTENTS CONTINUED

APPENDICES 65

APPENDIX A: AUTOMATION BOARD HEAT GENERATION 66
APPENDIX B: ELECTRICAL SCHEMATICS 69
APPENDIX C: LITERATURE REVIEW TABLE 69
APPENDIX D: SIMULATION SETUP PARAMETERS 83
APPENDIX E: MESA SHELL MANUFACTURING DRAWING 85
APPENDIX F: AUTOMATION CONTROL BOARD LAYOUT 87

LIST OF TABLES

Table Page

1. Health effects of common drinking water contaminates 9

2. Trial data from the emulated field test 53

C1. Table of references for literature review procurement 75

D1. Simulation initial conditions 84

D2. Parameters at the start of the simulation 84

D3. Simulation boundary conditions 84

LIST OF FIGURES

Figure Page

1. Historical average precipitation in Montana....3
2. Conventional soil-water sampling equipment with process steps....4
3. Primary biogeochemical cycles concerning dryland agriculture....11
4. EIS working principle and Randle's circuit....20
5. Hydraulic Schematic....23
6. MESA system implemented into an agricultural setting....25
7. Smart-Reservoir Module working principle....27
8. MSM fabrication steps....29
9. Multifunctional Sensor Module layout....30
10. 3D cutaway of MSM....31
11. 3D cutaway of CSM....32
12. Imported geometry and mesh for COMSOL study....35
13. MESA system with automation board and Prenart pump....38
14. Plot of real impedance for electrical conductivity measurements....40
15. Calibration curve comparison of various frequencies....41
16. Nyquist signature of three states in the packaging process....46
17. Calibration curve for the electrical conductivity sensor....43
18. Actual conductivity compared to calculated conductivity....44
19. Continuous conductivity measurements throughout the cleaning cycle experiment....48
20. Simulated cleaning cycle result....49

LIST OF FIGURES CONTINUED

Figure Page

21. Time series 3D plot of COMSOL simulation result 51

22. Results of the emulated field study 53

23. Proposed future sensor platform 56

A1. Infrared camera images of board during operation 68

B1. Control circuit used to drive vacuum pump and dispensing pumps 70

B2. Control circuit use to modulate valves 1 & 2 71

B3. Control circuit used to operate valve 3 72

B4. Level switch control circuit 73

E1. Manufacturing drawing for the acrylic shell 86

F1. Automation control board layout 88

ABSTRACT

Sustainable management of soil nutrients is a challenge for food production to meet the nutritional demands of a growing population of humans, which has surpassed eight billion. Informed management decisions toward maintaining suitable availability of plant macronutrients in soils without excess fertilizer inputs is limited by the ability to collect and analyze water chemistry in small sample volumes extracted from intact soils over time. Additionally, the semi-arid climate and increasingly more frequent meteorological drought conditions in soil systems like the agricultural regions of the Northern Great Plains limit the practicality of conventional soil-water collection and analysis techniques due to the small amounts of water available in the shallow vadose zone during the growing season.

In this work, I present progress toward a solution at the intersection of automation, microfabrication, and environmental monitoring systems. The Microfluidic Environmental Solute Analysis (MESA) system has the potential to allow multiple deployments providing enhanced spatial and temporal resolution compared to conventional soil-water collection techniques in measurements of soil water solutes critical to understanding the soil chemistry that supports agricultural production. Using only 100 µl of water extracted from the soil, the MESA system provides onboard, real-time electrical conductivity analysis (future work will include temperature, pH, and nitrate sensing).

The electrical conductivity (EC) sensor uses single-frequency electrochemical impedance spectroscopy (EIS) to measure the bulk fluid resistance within the measurement chamber of the MSM. Calibration of the MSM of EC ranging from 100 – 6440 µS cm^{-1} has shown that the cell constant is 9.530 cm^{-1}, although this parameter is sensor and package dependent. In-situ conductivity measurements in engineered soil columns have revealed that the sand tested has an intrinsic conductivity of approximately 380 µS cm^{-1}. The maintenance-free system is intended to be buried in the soil and provide automatic measurements throughout the Montana growing season without being disturbed. The deployment of the MESA system can provide researchers with new data that may enhance our understanding of biogeochemical cycling in dry-land agricultural settings.

INTRODUCTION

Background & Motivation

The human population grew dramatically at the dawn of the Neolithic Revolution about twelve thousand years ago when humans invented agriculture [1]. High-calorie foods became more abundantly available at this time, and humans did not have to travel long distances in search of food. The birth rate began to increase sharply, and the population has grown from approximately six million to eight billion since the introduction of agriculture, which represents a 1300-fold increase in the most recent 4% of human history [1]. Conservative estimates project the global population to reach ten billion by 2100 [2]. Rapid population growth has pressured agricultural practices to keep up with this growing demand. Consequently, agricultural lands expanded, and the current application of fertilizers per year is three times greater relative to rates used in the mid-1970s [3].

The concept of Planetary Boundaries (PBs) has been introduced help the public understand the effects of rapid population growth and increases in biochemical flows [4]. The seven PBs represent the facets of human intervention upon the balance of the Earth's stability. By 2015 humans had already exceeded the biodiversity and nitrogen biochemical flux limits set forth by experts [4]. Agricultural expansion has caused the largest impact on reduced biodiversity on Earth and has also had a major impact on nitrogen chemical flux limits. For every eight temperate grassland habitats converted for agriculture, only one grassland habitat is protected. Rapid deforestation for agriculture in the tropics since the 1990s has undeniably impacted [5] The increased demand from an ever-growing population drives the expansion of agricultural land.

The PBs are intended to provide thresholds in global biochemical fluxes that protect against the eutrophication of freshwater and marine ecosystems [4]. Eutrophication is the process in which a body of freshwater becomes over-enriched by nutrients such as Nitrogen (N) or Phosphorous (P) that leads to excess production of biomass that ultimately led to excess biological oxygen demand and hypoxia [5]– [7]. These issues lead to a decrease in available fresh water as a beneficial resource for humans and other animals, further compounding the issue. Anthropogenic input of bioavailable inorganic N such as nitrate and ammonium to Earth systems is disproportionately driven by the application of fertilizers such as urea within the agricultural industry [4], [8]. Nitrates are also being add to the environment from animal and human waste streams [9], [10]. Metal working factories use nitrogenous compounds in the production of stamping dies. Mismanaged waste leads to the dispersion of these compounds into the environment [11].

Although nitrogen (N) has adverse environmental effects when dispersed into waterways, N is crucial to the growth of crops such as wheat in Montana. 4.7 million acres of wheat are harvested yearly in Montana, representing a 1.1-billion-dollar industry [12]. Wheat is one of the largest economic drivers in the state of Montana and so her freshwater resources and soil quality must be protected from eutrophication, salination and soil acidification. Most of Montana's wheat is grown in the golden triangle or platinum rectangle, as shown in Figure 1. These regions are also particularly dry landscapes, and this makes conventional soil-water sampling methodologies difficult or sometimes impractical. In a climate that may receive only 13-25 cm of precipitation per year [13], there often is limited water available in the soil for chemical analysis.

Conventional methodologies using sampling with tension lysimeters shown in Figure 2 are labor-intensive, time-consuming, and sometimes impractical in under drier soil condition.

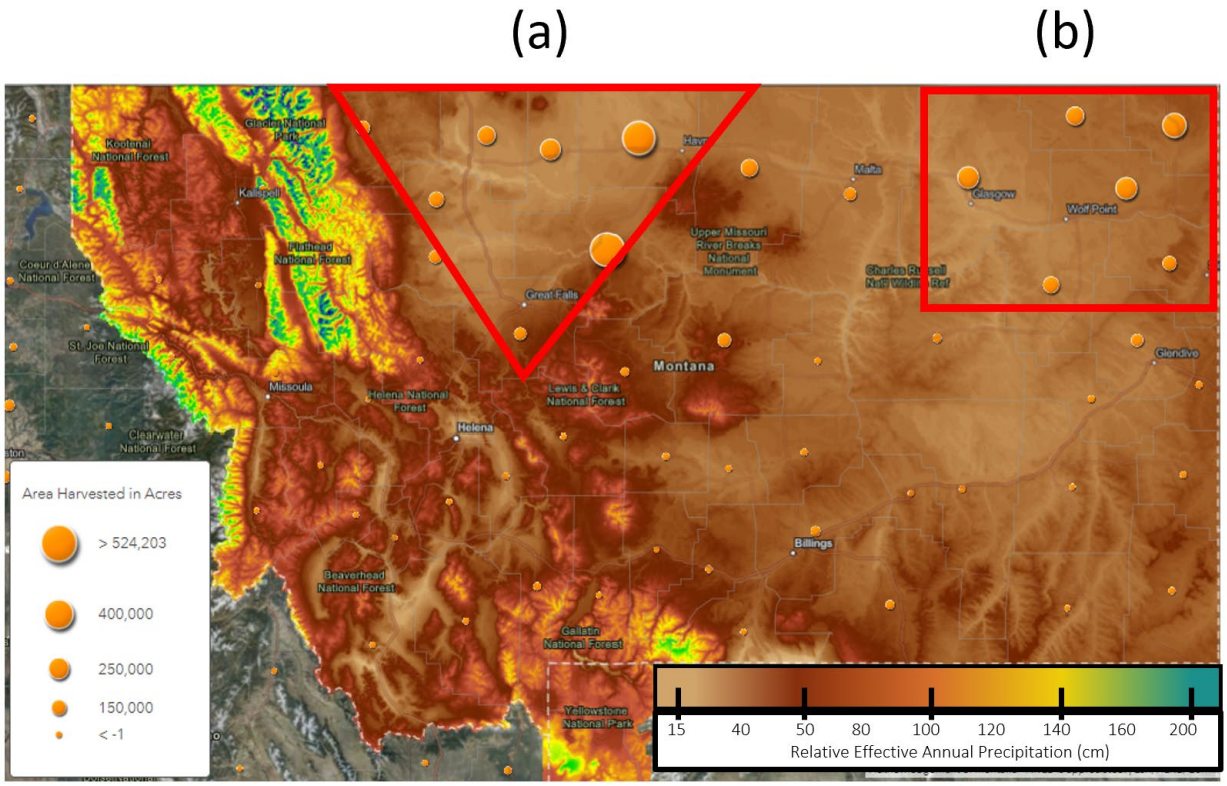

Figure 1: Relative Effective Annual Precipitation (REAP) for Montana (color gradient) and wheat acres harvested (orange dots) [14]. Historically, north central Montana may receive as little as 15 cm of precipitation annually and is known for growing Hard Red Winter Wheat in semi-arid conditions (a). Northeast Montana is less dry and primarily grows Dark Northern Spring Wheat and legumes (b). Data provided by the Natural Resources Conservation Service Montana State Office (NRCS) [13]. Precipitation data from University of Montana for the past 30 years has been sensitized to the landscape according to slope, aspect and known vegetation breaks.

Conventional soil-water sampling methodologies have limited the understanding of nutrient transport in soil systems. Sample transportation and handling (Figure 2, step IV) may introduce uncertainties derived from sample instability or contamination. In previous research in the Judith River watershed (JRW), researchers were unable to perform a complete analysis for

over 200 collected field samples due to limitations in sample volume (under 2 mL). Approximately 100 additional prospective samples were too small for the researchers to physically handle [15]. Extraction of volumes of water at the microliter scale from the soil and immediate subsequent analysis is not possible with current soil water monitoring technology.

A tool for high-frequency monitoring of water quality in soil pore waters of semi-arid regions will profoundly improve understanding of the biogeochemical transformation occurring during dry periods and the transport of solutes during wetting events. The magnitude of tension applied to the soil matrix is a key factor in understanding the fluid mechanics of soil-water movement in porous systems.

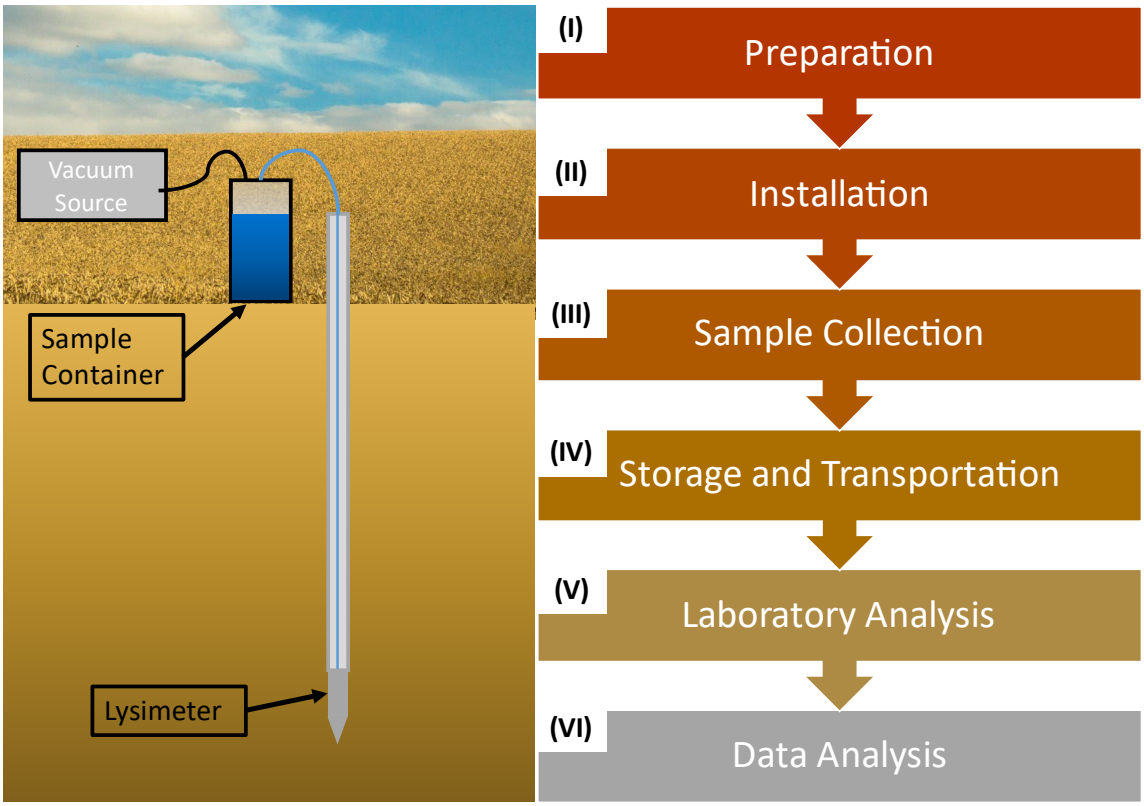

Figure 2: Conventional soil water sampling equipment and process. Standard soil water sampling arrangement is shown on the left. Six steps required to measure an ion such as nitrate with this tool are shown on the right. Adapted from the work of Wilson [16].

The character of soil is notorious for dramatic spatial variation, so the ability to collect data at a high spatial resolution is of interest to scale observations to larger plots or landscapes. Minimization of instrumentation production methods is desired to allow soil science or management practitioners to maximize deployment of multiple systems across an agricultural landscape. To reduce operation costs of monitoring networks, the system must be operable remotely, at least without excavating the system, [16].

Research Goals & Objectives

The challenges underlying monitoring soil pore water chemistry at high frequency and under drier conditions have motivated this research on the design and manufacture of a Microfluidic Environmental Solute Analysis (MESA) system. The main goal of this research is to design a micro-electromechanical systems (MEMS) device that will allow the production and testing of a proof-of-concept prototype of an automated soil-water sampling and analysis probe. Where possible, 3D printing was used as the primary manufacturing technique for custom parts to reduce the cost of production. Four specific objectives represent critical progress toward the ultimate goal of an autonomous deployable device:

1. Design a lysimeter integrated system capable of collecting a 100 µl sample from soil, analyzing that sample with a packaged microsensor, and self-cleaning to prevent memory artifacts.
2. Use Computational Fluid Dynamics (CFD) to study the potential chemical impacts of previous samples in the transient behavior of the cleaning procedure.
3. Create a custom circuit board control system that can be programmed to orchestrate the operation of all pumps and valves in the system.

4. Provide proof-of-concept tests of the systems functionality in an emulated field sampling environment, and document heuristics for the next iteration of design. This test should investigate the relationship between applied tension and extraction time as well as investigating the contribution of ionic compounds from a test soil.

Work in designing the probe aims to expand packing techniques for MEMS biosensors and provides a low-cost, simple, and ergonomic design that can be implemented in field research activities. The system requires autonomous control of the pumps and valves responsible for transporting fluid, prompting the construction of a custom printed circuit board (PCB) and installing the appropriate semiconductors and integrated circuits (ICs). The Arduino UNO (REV3) is a low-cost microcontroller unit and was integrated into the PCB design (see Appendix F). The final objective is to investigate the performance of the newly developed system by extracting water from soil that has been set to field capacity with a known conductivity.

A Review of Current Automated Water Analysis Systems

Autonomous *in-situ,* soil-water extraction systems have been introduced in the literature allowing for ease in duplicating experiments, collecting samples during varied metrological events, and minimizing disturbance. Reck *et al.* have developed a system capable of extracting soil-water samples in the vadose zone [17]. This system has the potential to analyze ions that have the potential to contaminate freshwater resources. However, the system has a large footprint and will require additional equipment to support on-site chemical analysis. Components of the work by Reck *et al.* may prove to be useful in future deployment of the MESA system.

A few examples of autonomous nitrate sensing systems have been designed for deployment in the sea [18]– [20]. The system developed by Beaton *et al.* uses a miniaturized version of the

Griess reduction process to measure the nitrate contents of sea water taken into the microfluidic chip [19]. This system uses a network of surface mounted Lee Company valves to manage the sample and reagents. The innovations from Beaton *et al.* have influenced the design and process flow of the MESA system. Recently, a mobile lab-on-a-chip device was developed to leverage microfabrication technologies and capillary electrophoresis (CE) to measure concentrations of NO_3^-, NH_4^+, K^+, and PO_4 [21]. This device is the only system mentioned that demonstrates the transduction of multiple ions on a single platform. Additionally, this system is designed to be used in the field to analyze soil-water extracts. Though, the operation of this system requires the use of a syringe pump to generate 100 kPa and a power supply capable of generating -2000 V. The equipment required to operate the CE system is not suitable for a miniaturized and low-power consumption system.

To our current knowledge there is not a system that can autonomously extract soil-water from the vadose zone and perform immediate analysis is dry-land agricultural systems; though, the concepts and research posed in recent years can provide relevant insight to realize a system capable of expanding the state-of-the-art.

Soil Nutrient Management and Drinking Water Quality

Research in the northern Great Plains has shown that ultra-fine textured soils in the Judith River watershed (JRW) are unable to store precipitation because the water is lost to percolation. Thin soils in this region were shown to exhibit nitrate leaching rates five to 16 times greater than thicker textured soils. The nitrate levels measured in this region exceeded the regulations set by the EPA, shown in Table 1 [15]. Ongoing fieldwork in the JRW to investigate NO_3^- contamination has an impact on the local community. Residents of the JRW area and the

producers who cultivate the land are important to the management of future work and the communication of experimental results. Qualitative and quantitative results suggest that research efforts in the JRW have positively impacted the community by improving the understanding of the role of agricultural management in water quality [22].

Biogeochemical reactions and hydrologic flows governing the fate and transport of solute in porous media dictate the mechanisms by which freshwater becomes contaminated within terrestrial ecosystems. Chemical cycling in soil systems drives how atmospheric nitrogen transforms through microbiological fixation, mineralization, and nitrification into the more stable but still plant available form of nitrate (NO_3^-). Despite being biologically active, nitrate is a longer-lived species of inorganic nitrogen, where natural precipitation events and irrigation practices can transport soluble ions from the rooting zones in the cropping system into regions of water accumulation such as aquifers or preferential flow paths. Nitrate, naturally occurring salts, and hydroxyl groups are highly soluble ions and can contaminate freshwater resources, including human drinking water sources, by leaching. Soils tend to become saline in systems with high leaching rates [23].

Nitrogen fertilizers (most commonly urea) are applied to crops to increase yield and improve profit margins. When applied in excess of crop demand, this nitrogen may follow multiple microbial metabolic pathways to become nitrate as shown in Figure 3. Crops such as wheat will use nitrate within the rooting zone, but nitrate is highly soluble and non-sorptive and is likely to be transported deeper into the soil profile during wetter conditions. Hydrogen ions are by-products of the nitrification process facilitated by nitrifying bacteria [24], decreasing the pH.

When soil pH falls below 5.5 heavy metals such as aluminum are released into the soil and interacts with the crops root structure, decreasing yield efficiency [25].

It is important that the water humans drink is clean and free of contamination which can cause adverse health effects. The Environmental Protection Agency (EPA) has published standards as a Safe Drinking Water Act (SDWA) requirement. These standards are referred to as the National Primary Drinking Water Regulations (NPDWRs) to protect public drinking water from the following groups of contaminants: microorganisms, disinfectants, inorganic compounds, organic chemicals, and radionuclides [26]. Contaminates relevant human health are shown in Table 1. The inorganic compound nitrate is considered a serious contaminant for potable water because long-term consumption over the established limit may increase the risk of colorectal cancer [27]. Nitrate contamination in drinking water is the primary cause of methemoglobinemia (blue-baby syndrome) in infants who consume water with excess nitrates. When nitrate enters the digestion track, nitrate-reducing bacteria convert the nitrate to nitrite and react with hemoglobin to form methemoglobin [28].

Table 1: Health effects of common drinking water contaminates and their sources. Drinking water standards compiled from EPA regulation 816-F-09-004 [26]

Contaminate	**Drinking Water Standard**	**Possible Health Effects**	**Contamination Sources**
Nitrate	Must be less than 10 mg/L NO_3-N	Cancer risk [27], Methemoglobinemia [28], [29]	Fertilizer run-off, leaching, sewage, industrial, nitrification
pH	Less than 8.5 and greater than 6.5 is recommended	Diarrhea, nausea and vomiting, organ failure (heavy metal toxicity) [30]	Industrial, leaching, nitrification, rainfall
TDS	Less than 500 mg/L is recommended	Cardiovascular disease, diarrhea [31].	Leaching, weathering

Hemoglobin is responsible for transporting oxygen to tissues, but methemoglobin does not easily bind to oxygen molecules. As the illness progresses, bodily tissues become asphyxiated and turn blue [28], [29].

The EPA has placed the pH drinking water standard in a non-enforceable regulatory guideline called the National Secondary Drinking Water Regulation (NSDWR). The contaminates included in the NSDWR are regarded as substances that can cause cosmetic or aesthetic effects, including but not limited to taste, odor, color, or skin irritation. The pH of the water alone is not explicitly harmful; however, the externalities of acidic corrosion included copper and lead consumption. These metals have exposure limits in the NPDWR of 1.3 and 0.015 mg/L [26] Acidic water ($pH < 6.5$) can corrode metal pipes in drinking water systems and leach toxic metals into the flowing liquid. In severe cases, heavy metals can taint the freshwater source and harm humans, causing diarrhea, nausea, vomiting and even liver failure [30].

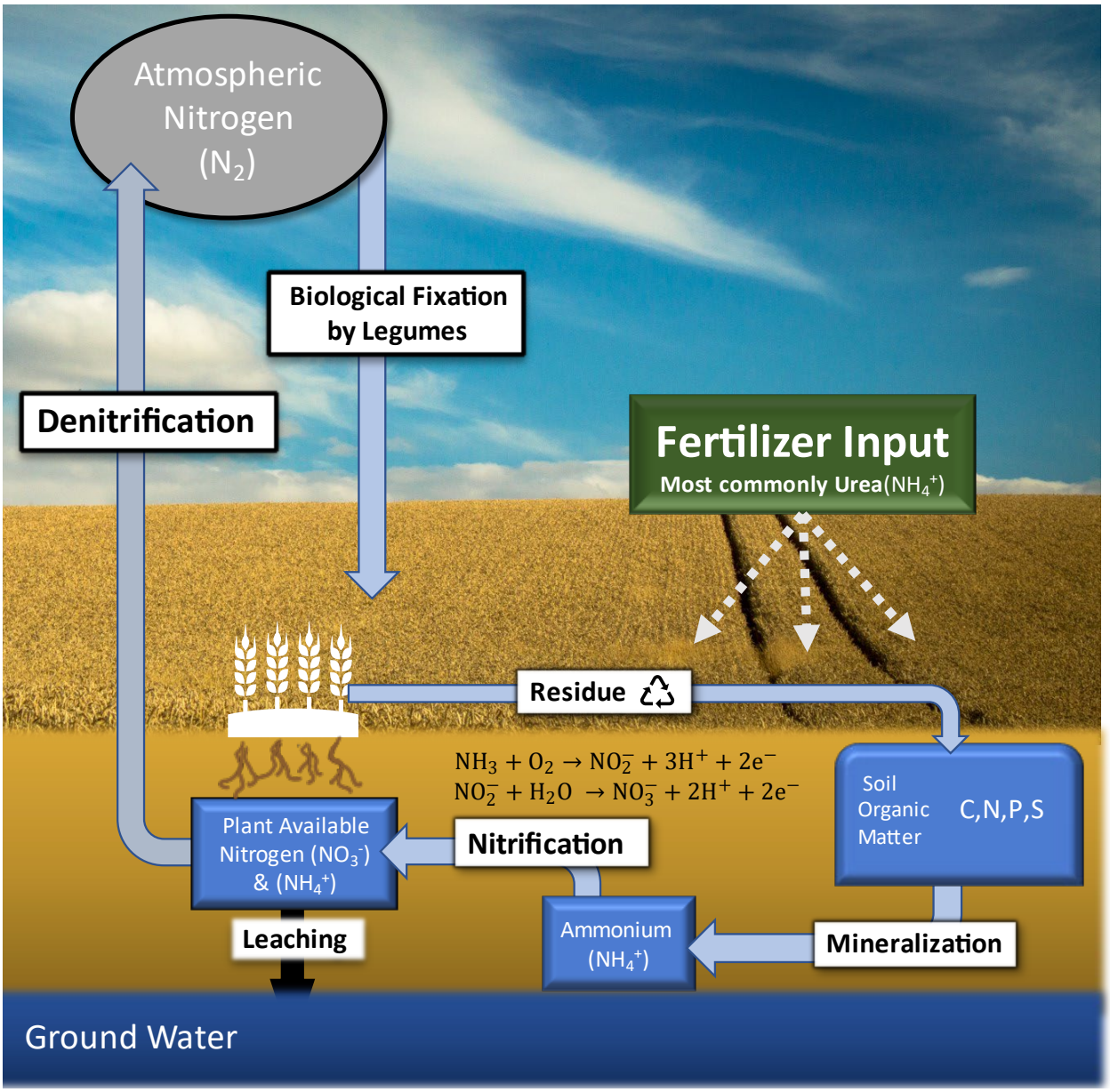

Figure 3: Primary biogeochemical processes which affect dryland agricultural systems. This simplified model shows the relevant pools and fluxes to this research.

An Evaluation of Existing Microsensor Technologies for Environmental Monitoring

Today there is increased interest in and demand for transducers capable of measuring water quality and agronomy chemicals. Research and development of nitrate, pH, and electrical conductivity sensing devices are important because they have utility in the disciplines of water quality, soil health, and crop yield efficiency. Although, several transduction principles with varying benefits have been used in previous work as miniaturized analytical chemistry tools in natural water, such as optical (absorbance and colorimetry) and electrochemical (potentiometric, voltammetry/amperometry, electrochemical impedance spectroscopy). Typically, electrochemical sensors are solid-state and feature miniaturized footprints. While some optical sensors outperform many electrochemical devices, they often require complementary hardware and chemical reagents for operation. Regardless of the sensing mechanism or measurement principle, the range, limit of detection, and platform size are important to consider for successful integration within an *in-situ* monitoring system. To fully comprehend the advantages and disadvantages of current and emerging sensor technologies, the following review will support future sensor platform designs.

Optical Transducers

Sensors have been developed to transduce optical signals to interpret chemical species concentrations. The primary methods in the literature are absorbance and colorimetry. The core of these sensing principles is to relate the light interacting with the sample to the relative chemical concentration of interest. Optical sensing chemical analysis systems promote lower limits of detection and improved accuracy, although these solutions often present large

apparatuses with complex layouts and additional hardware requirements. Significant efforts have been made to produce portable, low-cost nitrate detection systems.

Absorbance: Engineering innovation in 2021 [29] produced the unique portable UV-absorbance analysis tool. The low-cost system used the 12 MP camera featured on the Apple iPhone Xs Max to capture images of the light pattern. Nitrates absorb light in the UV-C range from 195-210 nm, prompting the use of a bandpass filter. Post-processing steps inform the researchers of the intensity of the light, which is then related to the nitrate concentration level by the Beer-Lambert Law. This system detected nitrates with an accuracy of 0.2 ppm with a linear range of 0 – 5 ppm NO_3^- -N. The benefit of absorbance systems is that the selectivity can be easily tuned since molecules absorb light at different wavelengths. The range of this system is narrow; however, the cost is much less than commercially available nitrate detection systems. Rather than filtering the light used to interact with the sample, it is possible to mix graphene oxide nanocomposites and gold nanoparticles (GNP) with amino groups and cause disaggregation of the GNP as a function of the nitrate level. When the GNPs separate, the light is more easily transmissible through the background media, and a photodiode can measure this change [30]. This mechanism is extremely sensitive (0.072 NO_3^- -N limit of detection) but requires more work to implement the technology into a system. Engineers will continue to expand this area of research and provide new and improved absorbance systems for chemical analyses.

Colorimetry: The colorimetric detection of nitrate commonly uses a procedure first developed in 1858 by Peter Griess [32]. The Griess test requires a reagent to be mixed with solution containing nitrite (NO2) to change color. However, this extremely sensitive detection

principle requires nitrate to be reduced to nitrite. The chemical reduction process is typically completed with a cadmium tube-like component.

Efforts in 2021 have been made to miniaturize the Griess assay. The system uses a three-dimensional polydimethylsiloxane (PDMS) based micro-mixer to combine the sample with the appropriate reagents to carry out the reactions. The PDMS microstructure, which incorporates zinc and cadmium-coated blocks to react to nitrate to form nitrite. Second, the newly formed nitrite solution interacts with the Griess reagent. This miniaturized system exhibits rapid detection times (115 seconds) and a linear range of 0 –718 mg/L NO_3^- -N. Additionally, the system showed to have a limit of detection (LOD) of 0.718 mg/L NO_3^- -N [20]. Other environmental science and technology researchers have created similar systems capable of using the Griess test.

Electrochemical Transducers

Ion Selective Electrodes: One of the most common electrochemical sensors for the detection of plant macronutrients is the ion-selective electrode (ISE) [33]. These active transducers have an engineered material called the ion-selective membrane (ISM), which converts the target ion's activity into an electromotive force (EMF). Potentiometry is used to measure the EMF relative to a reference electrode and is related to the concentration of ions in the solution. Nitrate sensing ISEs have recently been improved to provide wide detection ranges, low limits of detection, and long-term stability. In a recent study by Ali *et al.* [34], a newly developed nitrate ISE was shown to have a range of 2 – 1500 ppm NO_3^- -N and a limit of detection of 1.3 ppm NO_3^- -N. Notably, this sensor incorporates a unique nanocomposite (POT -MoS2) as an ultra-sensitive ion-to-electron transduction layer. The POT-MoS2 nanocomposite

was shown to provide a super-Nernstian sensitivity of 64 mV/decade. The miniaturized sensor was shown to have good stability for an extended duration of 27 days. The sensor platform incorporates the ion-selective working electrode and an Ag/AgCl reference electrode. The reference electrode is a requirement for potentiometric transducers, thus increasing the sensor platform size and complexity. Additionally, this sensor requires the substance nitrocellulose to manufacture the ISM. Nitrocellulose is known to be explosive and dangerous to work with in the absence of specialized safety controls. Alternative ISM compositions have been proposed as well, such as nitrate doped polypyrrole, abbreviated PPy (NO_3^-) and Cobalt (II) 4,7 – Diphenyl-1,10 – phenanthroline [35], [36] These devices present similar performance specifications to [34] while using materials that are safer to handle. Other nitrate-sensing ISEs have been produced in recent years with moderate performance capabilities and simplified ion-to-electron transduction layers [37]– [39].

Voltammetry: An alternative measurement technique applied to selective microsensor platforms is voltammetry. In voltammetric measurements such as linear sweep voltammetry (LSV), the potential applied to an electrode or electrode array is increased in one direction while measuring the response current. A nitrate microsensor was developed in 2019, which uses LSV to measure the concentration of nitrate ions within a range of 1 – 15 mg/L ($R2 = 0.99$) with a LOD of 0.074 mg/L (NO3- -N). This nitrate sensor has thirty pairs of platinum-interdigitated electrodes modified in two secondary surface deposition steps. First, palladium (Pd) was electrochemically deposited on the working electrode using a constant voltage to form a spherical topology. Second, gold nanoparticles (AuNPs) were deposited atop the palladium with

a constant voltage resulting in a dendritic structure with a high surface area, enhancing the sensitivity.

The final Pd-AuNP alloy interacts with nitrate ions by reducing nitrate to nitrite and improving the catalytic activity of the thin-film sensor. Using LSV, the current response changes with increasing nitrate levels without being affected by other ions such as chlorine, sulfate, or carbonate [40] Similar devices that leverage redox activity enhancements have previously been fabricated using metals such as silver, gold, or copper in conjunction with an ultra-sensitive microstructure such as nanoparticles or dendrites. These devices use other voltammetric measurement processes such as cyclic voltammetry (CV), square wave voltammetry (SWV), or differential pulse voltammetry (DPV) to measure enhancement in the response current to an excitation voltage across the electrodes [41]– [45].

Electrochemical Impedance Spectroscopy (EIS): EIS is another common electrochemical measurement technique found in the literature. EIS can be used to investigate phenomena occurring at the interface of the electrode and in the bulk material under test (MUT). Typically, the frequency is increased from low to high across an application-dependent range. The frequency range used in an EIS measurement depends on the MUT and can vary from the mHz range for solid-state materials up to several MHz for liquid samples [46] , an impedimetric sensor was developed for the detection of nitrates in a microfluidic flow cell. The device had a range of 0.442 – 442 mg/L and a LOD of 0.135 mg/L (NO_3^- -N). The electrochemical transducer uses a NiR/PEDOT NF-GO composite as a surface modifier to the gold working electrode [47] Poly(3,4-ethylenedioxythiophene) (PEDOT) has been shown to be an advantageous electron transducing layer due to its high conductivity, structural integrity, and biocompatibility [48]

PEDOT has been shown to have a positively charged polymeric backbone that promotes the coupling of enzymes such as nitrate reductase (NiR). Graphene Oxide (GO) enhanced the sensitivity of this nitrate sensor from 24.35 Ω/(mg/L)/cm2 to 61.15 Ω/(mg/L)/cm2 by the addition of GO to the working electrode because of the composite's high surface area. EIS has also been used in past work as a measurement technique for pH sensors. Ruthenium Oxide (RuO2) has been shown by Mingels *et al.* to modify the electrical double layer due to interfacial reactions between the RuO2 and hydroxyl groups interacting with the sensor [49], [50] Zinc Oxide (ZnO) and tin oxide (SnO2) are also considered pH-sensitive materials. EIS sensors using these materials have been created, although the range of these devices is not acceptable (1- 7 pH), and the measurement error is considerable [51].

Electrical conductivity (EC) sensors have been created for environmental monitoring applications using single-frequency EIS. Auto-ranging has been made possible by board-level switching to vary the equivalent circuit with auxiliary resistors and capacitors. The range of a device leveraging this technology is 0.5 to 20,000 μS cm^{-1}; however, this device is bulky [52]. EIS EC sensors can be manufactured with microfabrication technologies to have miniaturized footprints. Manufactured by Lin *et al*., their circular, 2-electrode EIS sensor has a range of 100 – 8000 μS cm^{-1} [53].

In this work, a similar design to Lin *et al.,* was used, although the electrodes were manufactured with gold rather than platinum. The applicable range for EC in agricultural applications is understood to be 100 -5000 μS cm^{-1}, and so the design by Lin *et al.* is sufficient. If the application requires the range to be adequate for seawater research, it is possible to microfabricate a 4-electrode sensor to enhance the range. These 4-electode devices use the outer

pins to source current while measuring the voltage between the two inner electrodes. This modification of the EIS technique exhibits a high input impedance of the voltage measurement circuit and prevents influences from charging currents or polarization of the electrode-electrolyte interface [54].

Summary

Sensitive and miniaturized measurement systems for environmental monitoring have become more common in the past 20 years following advances in microfabrication technologies. For a complete collection of sources used in the creation of this review, see Appendix C. Although several examples of miniaturized nitrate sensing devices have been described, two stand out as viable options for implementation in the MESA system. Soft lithography, thin-film deposition tools, and the rise of integrated circuits have made nitrate sensing technologies such as the optical system by Wang *et al.* [20] possible. The Wang *et al.* solution to nitrate sensing presents a low LOD and wide range applicable to freshwater and seawater analysis. Unfortunately, this system is bulky, requires the storage of reagents, and is only selective for one analyte. The miniaturized nitrate sensor developed by Ali *et al.* [47] demonstrates acceptable performance specifications while dramatically reducing the footprint, cost, complexity, and additional hardware. In addition, the modified interdigitated electrode pH sensor developed by Mingels *et al.*[49] is a design that could be implemented on a future sensor platform in the MESA system.

Fundamentals of EIS

Electrochemistry grew in popularity in the early 20th century, and leaps in scientific understanding proliferated among great scientists and engineers [46]. Electrochemical impedance spectroscopy, or EIS is a holistic electrochemical analysis approach that works by sourcing a sinusoidal current through a known resistive element, producing a controlled voltage drop. The ratio of the voltage applied to the electrodes structure to the complex measured current response is, quantitatively, the impedance, as shown in Equation 1. In principle, Oliver Heaviside theorized in the 1880s that impedance is made of capacitive and resistive components [46]. The portion of the measured signal which is out of phase contributes to the capacitive impedance response, and the piece in phase is the resulting resistive impedance response. The impedance Z follows ohm's law; the ratio of the complex electrode voltage (V) at frequency (ω) divided by the complex response current 'I' and accounting for the phase shift 'θ' ($j = \sqrt{-1}$ denoting complex terms).

$$|Z| = \frac{V\, e^{j\omega t}}{I\, e^{j(\omega t - \theta)}} \tag{1}$$

Separate the in-phase, real portions of Z and the out-of-phase imaginary portions of Z to obtain Z_{REAL} and $-Z_{IM}$, as shown in Equations 2 and 3.

$$Z_{REAL} = |Z| \cos\theta \tag{2}$$

$$-Z_{IM} = |Z| \sin\theta \tag{3}$$

The impedance vector is drawn on an x-y plane with real numbers on the x-axis and imaginary numbers on the y-axis. Capacitive impedance is expressed by an imaginary number and resistive

with a real number. Electrode-electrolyte interfacial reactions are characterized by modifications to the so-called double layer capacitance denoted C_{DL} and charge transfer resistance R_{CT} shown in Figure 4.

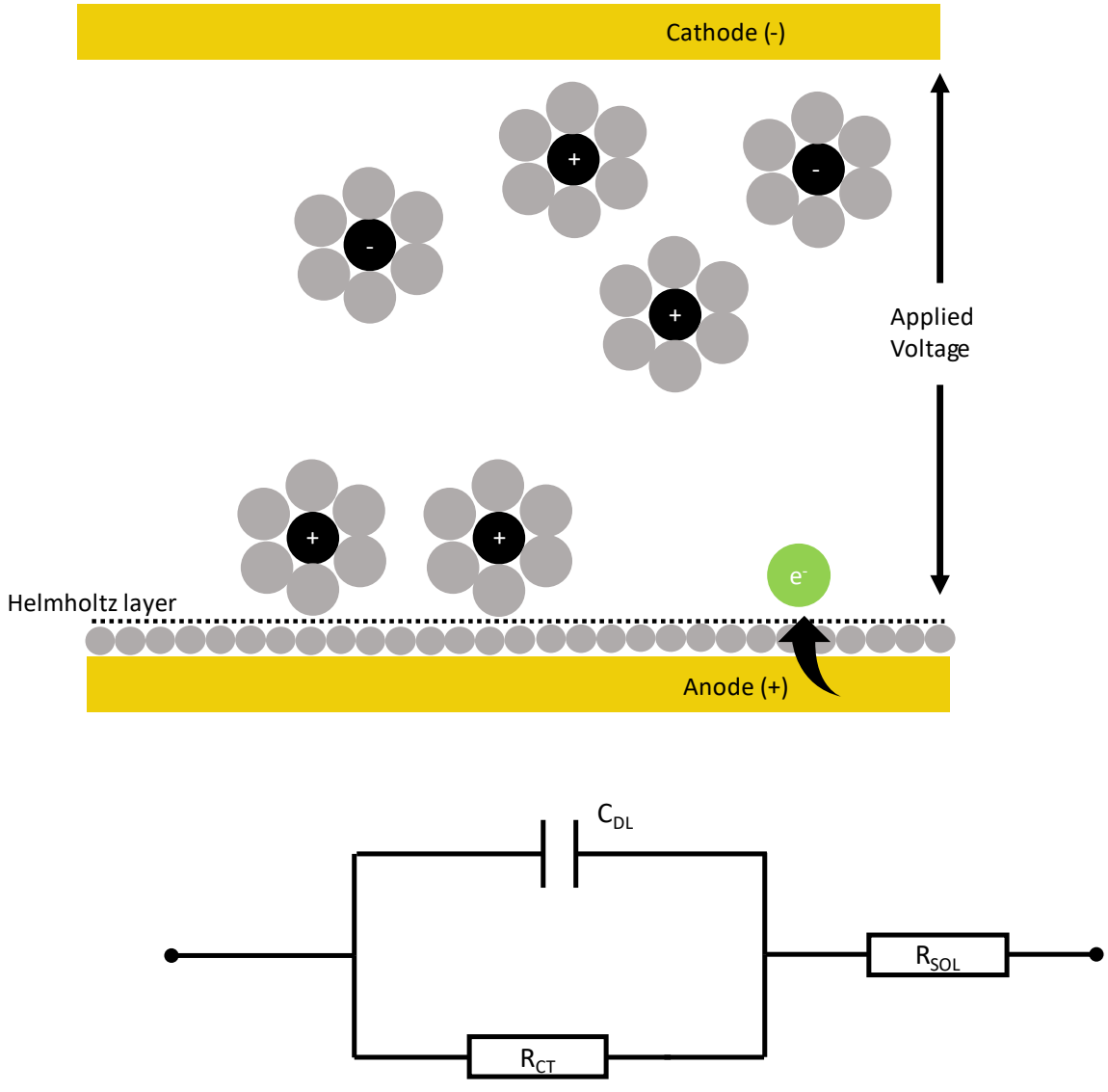

Figure 4: EIS working principle and equivalent circuit. Inspired by the work of Lvovich [46]

The current generation and discharge process occurring in the nanometer thick "Helmholtz" layer drives the transduction principles leveraged in work described above as EIS nitrate and pH sensors from Ali *et al.* and Mingels *et al.* During an EIS measurement, the excitation frequency is increased through a broad spectrum to investigate the nature of the electrochemical surface interactions and the bulk solution properties. EIS has become an increasingly popular analytical tool because of the breadth of applications and holistic insight into the system.

For EIS measurements of ionic solutions, the magnitude of the bulk solution resistance is shown in Figure 4 as R_{sol}. The bulk solution current is dominated by the migration of electroactive species such as ionic salts. Across the appropriate frequency ranges, R_{sol} may be calculated by using Equation 2. At high enough frequencies, the impedance of the C_{DL} decreases to near zero, and the applied current flows dominantly through the R_{sol} element in Figure 4. Deploying electrical conductivity sensors in the field for real-time determination will be the first step in a new age of environmental monitoring tools.

MATERIALS & METHODOLOGY

MESA System: Description

The MESA system has been designed to meet the specifications of the following level-one requirements: extract a soil-water sample with a volume of 100 µl or less, incorporate a microsensor for onboard chemical analysis, integrate a porous cup lysimeter for sample extraction, self-clean, and has a small footprint. For the first time, a porous cup lysimeter is incorporated into an automated soil-water extraction and analysis system. The Microfluidic Environmental Solute Analysis (MESA) system can collect high-frequency data to provide unique temporal resolution in agricultural environments. MESA employs advanced micro-sensor technologies coupled with 3D printing technology. This functional tool for environmental research will provide new perspectives regarding the transport of solutes in porous media to inform agricultural management schemes. Tension must be applied to the soil matrix from an external source to extract water held by the soil pores. As discussed, the industry standard for extracting soil water is to apply a vacuum to one port of a closed volume, two-port reservoir. The second vacuum line goes to a porous cup lysimeter that filters the water and connects the imposed vacuum to the soil. As the user applies tension to the internal volume, water is pulled from the soil pores and transported into the reservoir.

The MESA system employs the same logic but on a miniaturized scale with additional advanced features as shown in Figure 5. During the sample extraction process, a microcontroller starts a vacuum pump, and tension is applied to the MESA Smart-Reservoir module, internal capillaries, porous cup, and the soil in contact with the lysimeter. As time progresses, the water is pulled into the tubing network and deposited into the Smart-Reservoir drop-wise. In the Smart-

Reservoir module, a simple level switch is used to signal to the microprocessor when the Smart-Reservoir has reached the desired volume.

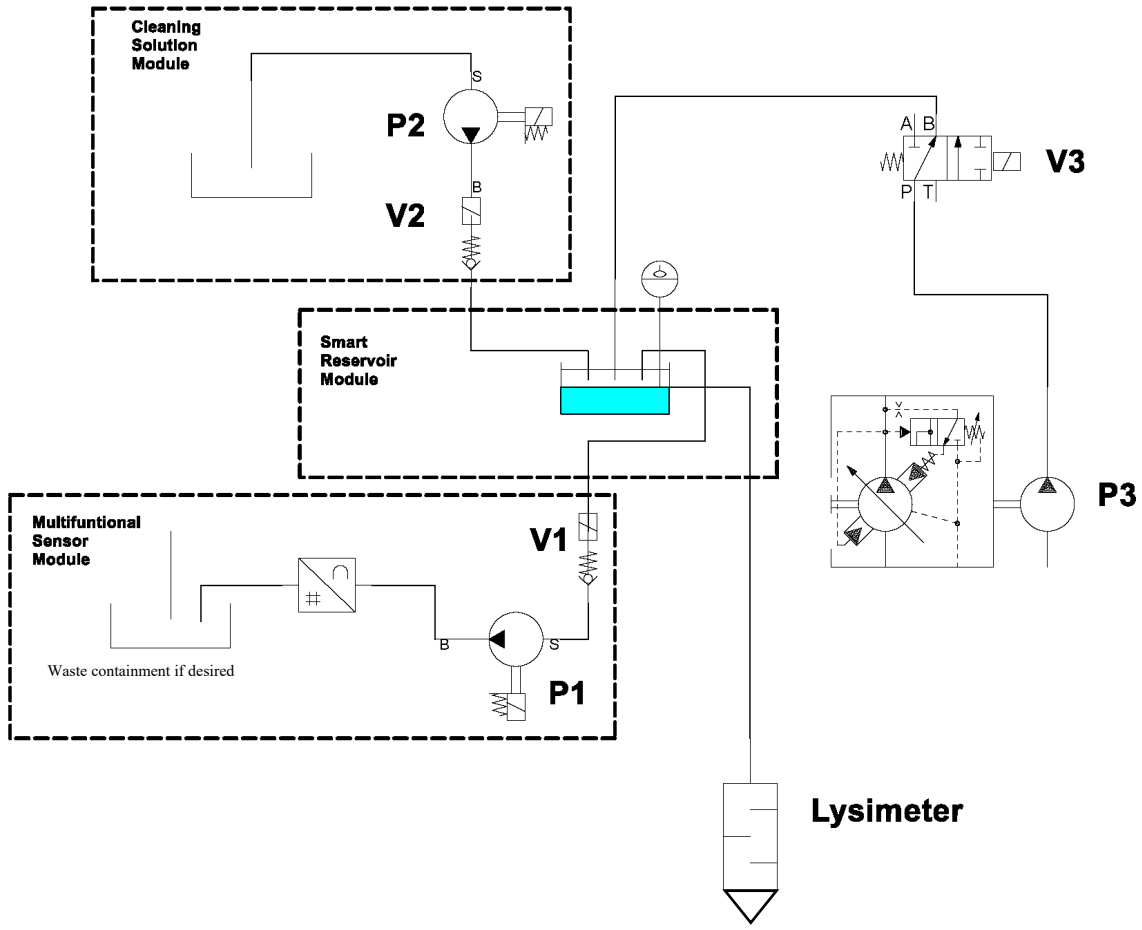

P1: Lee Company LMPX0501650B 10uL 12V

V1: Lee Company INKX0519850A 12V N.C.

P2: Lee Company LMPX0501650B 10uL 12V

V2:Lee Company INKX0508000A 12V N.C.

P3: Prenart Variable Rate Portable Vacuum Pump

V3: Lee Company LHLA1231380D 12V, 2 POS.

Figure 5: Hydraulic Schematic of the MESA system (created with Bosch Scheme editor 6). The microfluidic management components purchased from Lee Company are shown above. The lysimeter used for all experiments is a Prenart, PTFE/silica glass porous cup with an average pore size of 2 µm.

The MESA system requires the integration of a microfabricated sensor into a microfluidic channel network to process a 100 µl soil-water sample. The packaged microsensor is integrated with a Lee Company micro-dispensing pump which precisely infuses the sample water into the measurement chamber. A custom-printed circuit board (PCB) with spring-loaded pins is used to connect to the transmission lines of the sensor electrically. This complete package of components is the Multifunctional Sensor Module (MSM). These innovations allow for handling ultra-small fluid samples extracted from dry soils. Once the sample has been dispensed into the measurement chamber, the water's electrical conductivity is determined using a single-frequency electrochemical impedance evaluation. This measurement technique differs slightly from electrochemical impedance spectroscopy (EIS) and will be explained in detail in a future chapter. After the measurement is completed and the data is saved, the sample must be purged, and the system cleaned [55] An additional module is responsible for storing and transporting the cleaning solution.

The cleaning fluid (BIOPHARM conductivity solution, strength 100 µS cm^{-1}) is pumped into the Smart-Reservoir and then through the MSM. This step aims to wash out the previous sample to reduce the hysteresis error and prevent the precipitation of natural solutes or biologicals in the microchannels or micropumps. The core modules and miniaturized electronics are housed inside a weatherproof acrylic shell to protect the electronics from moisture and contamination. All MESA system internals were manufactured using LCD photoreactive resin 3D printing. Resin-based 3D printing technology allows for the fabrication of 100% max density, inexpensive plastic parts. The Computed Aid Design (CAD) models for each module and adapter were exported as a stereolithography file (STL) and sliced using the Anycubic Photon Slicer

V1.3.6. The part was built layer-by-layer from ESUN standard clear PLA resin. The Anycubic Photon printed all modules with 50 µm thick layers, 60s base cure time (5 base layers), 7.1 s normal cure time. After printing, the part was ultrasonically cleaned in a 95% isopropyl alcohol for 5 minutes, dried with compressed air, and cured in a 65W LED Ultraviolet oven.

An illustration of a fully assembled MESA system is depicted in Figure 6. In the future, researchers can use the MESA system to analyze chemicals found in dry-land agricultural settings with new temporal and spatial perspectives.

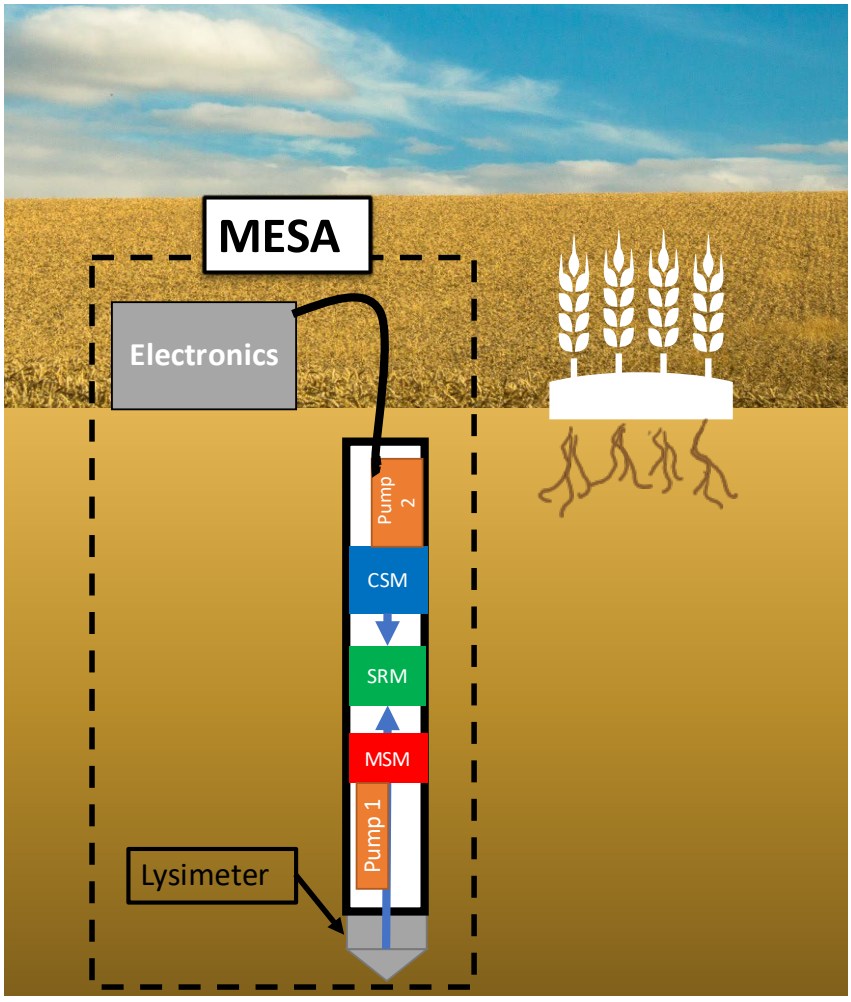

Figure 6: MESA system implemented in an agricultural landscape. The three core modules are depicted in the probe: CSM, SRM, and MSM.

Smart-Reservoir Module

The Smart-Reservoir Module (SRM) is designed to be an air-tight container for holding the soil-water extract. The SRM earned its name for the unique integrated level switch strategically placed in the container. The SRM can communicate electronically with the vacuum extraction pump by means of a simple analog circuit. The level switch sends a signal to a pair of wires arranged horizontally through the SRM, as shown in Figure 7. 50 kPa of negative pressure is applied to the internal volume of the SRM, connecting tubing and the soil-water sampler. Water moves through the soil into the sampler and finally to the SRM. As drops of water are deposited into the SRM, an analog signal is read between the level switch wires (facilitated by an Arduino UNO REV3). The analog signal is related to the resistance between the two wires but is not a deterministic value. Since air is much more resistive than water, the analog signal when the reservoir is empty (or filling) is distinguishably lower than when the water level physically surpasses the top wire. The top wire is strategically positioned with respect to the vertical cross-sectional area of the SRM to change the analog signal when the reservoir has precisely 100 µl. This feature is used to automate the soil-water extraction process by sending a signal to the system's vacuum pump to shut off when the SRM is holding 100 µl.

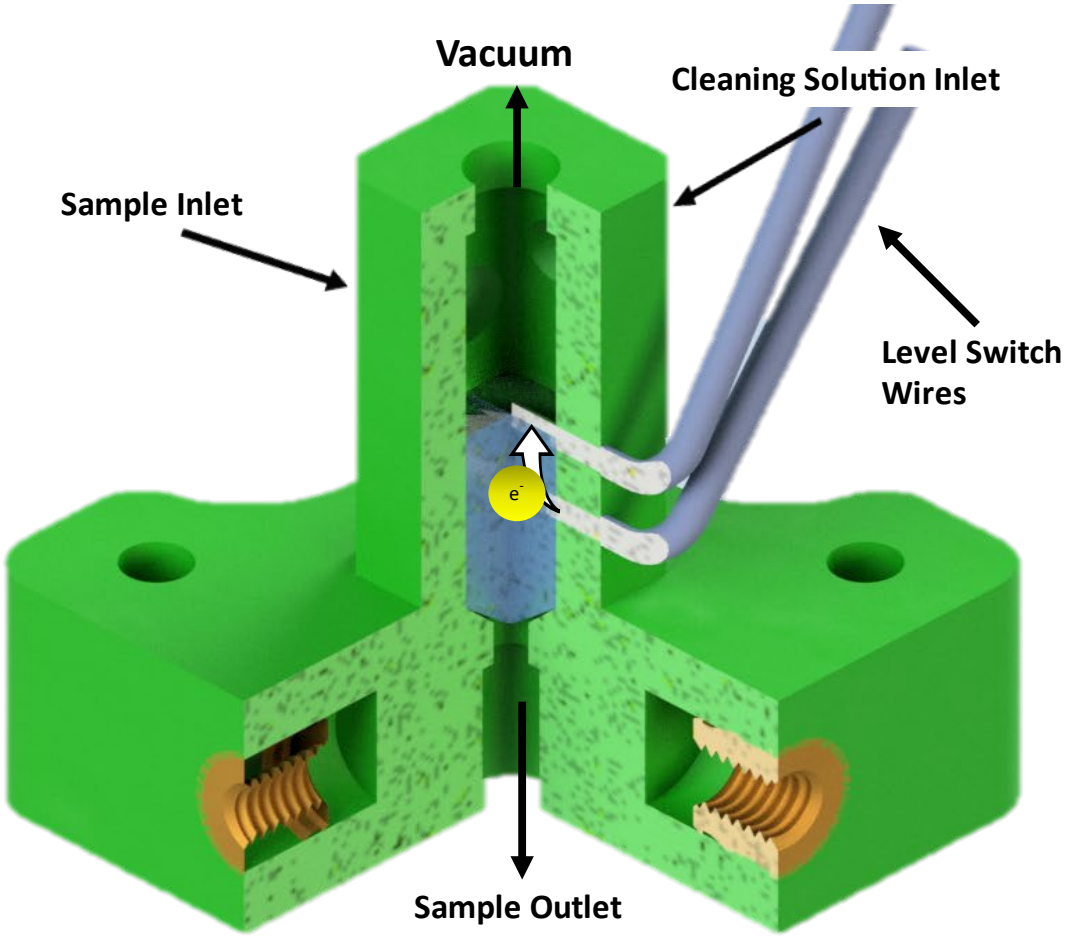

Figure 7: Smart Reservoir Module (SRM) configuration and working principle during the filling process.

Additionally, the SRM is used in the cleaning process as an intermediate residence for clean water. The same logical operation is carried out when filling the SRM with clean water.

Once the soil-water extraction process is complete, the internal vacuum is vented using a 3-position air control valve (Lee Company, magnetic latching, LHL series). This step is critical because it allows the air pressure to equilibrate with the atmosphere and allows for pumping into the Multifunctional Sensor Module (MSM).

Multifunctional Sensor Module

The Multifunctional Sensor Module is a 3D-printed sensor package used to electronically and fluidically connect the sensor electrodes to the sample water. The MSM incorporates a micro-electrical mechanical systems (MEMS) device, which is a chip and the focus of previous work related to *in-situ* sensing of biofilm formation in multiple applications including but not limited to space, industrial and icy environments [56]– [58]. 3D print orientation and internal channel geometry have been optimized to reduce the measurement chamber's internal volume to 27.8 µl. Figure 8 (I) shows the print orientation of the MSM. By printing the part in this configuration, the measurement chamber is as smooth as possible because it is parallel to the build plate and is the last layer printed. The multifunctional sensor shown in Figure 9 was treated with silane to enhance the bond strength between the borosilicate glass and the photoreactive resin, a process previously improved by Neubauer *et al.* The silane treatment protocol has previously been used to improve the adhesion of 3D print resin to glass for direct sensor integration [59]. In Neubauer *et al.*, sensor channel geometry was directly printed onto the substrate; however, in this work, the sensor is cured into the measurement chamber after the module is printed. The resin trench depicted in Figure 9 is strategically designed to capture any excess resin, preventing the resin from flowing on the sensing structures. The MSM uses heat-set brass thread inserts to accommodate the installation of a precision micro-dispensing pump (Lee Company LMPX series); this pump is referred to as P1 as shown previously in Figure 5. The purpose of this pump is to transport the soil-water sample from the SRM (discussed in the previous section) to the measurement chamber in the MSM. P1 is a 12-volt solenoid-driven diaphragm pump that operates at a dispensing frequency of 5 Hz and provides 10 µl ± 10% with each cycle. Bubble formation in the MSM does not affect the EC sensor but has been an issue

and will need to be addressed to ensure that chemical analysis may be performed with the additional electrode structures depicted in Figure 9 (b), (c). The measurement chamber geometry shown in Figure 10 has been optimized by smoothing the boundary edges in accordance with a comprehensive review on bubble nucleation [60]. Additional methods may be employed to eliminate bubble formation all together such as phase guides and hydrophilic surface enhancement [61].

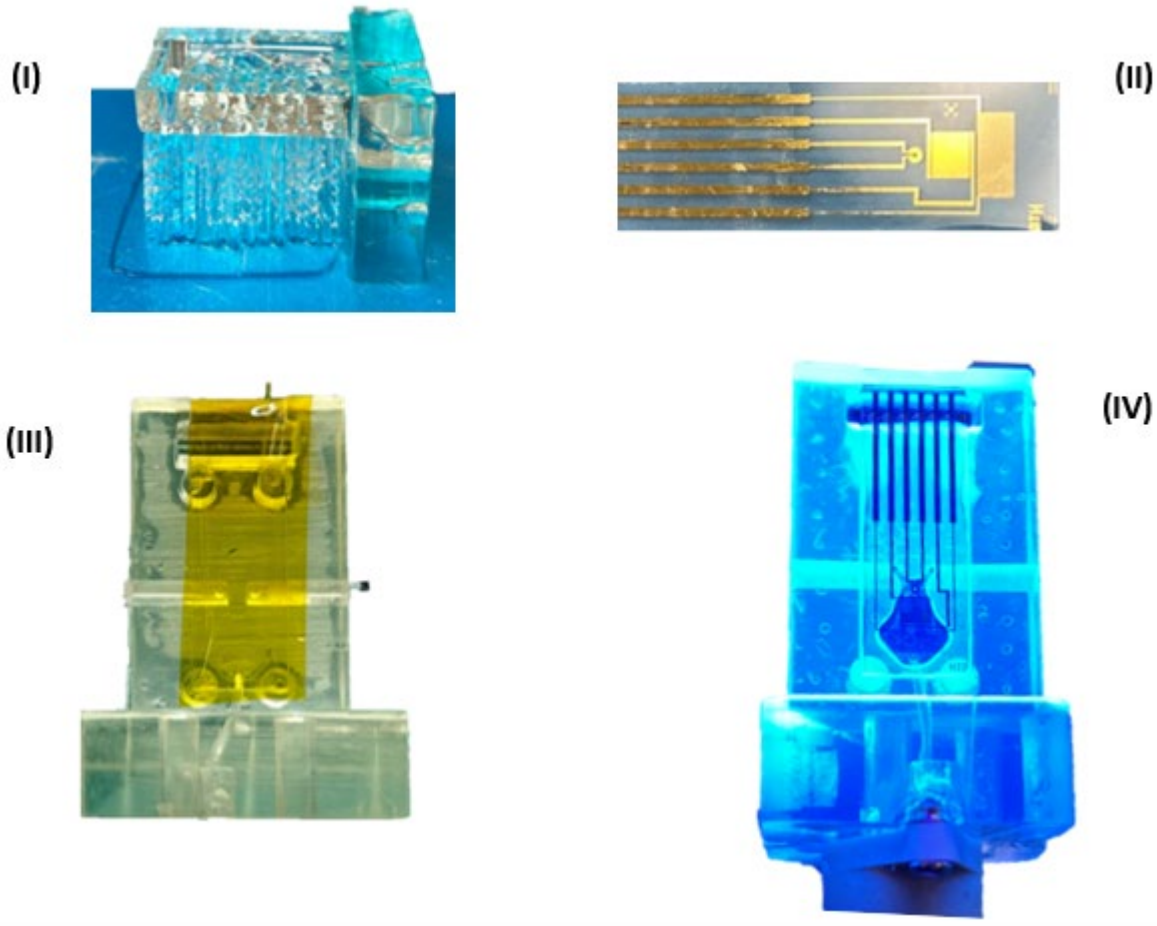

Figure 8: MSM Fabrication steps. 3-D print the MSM in the orientation shown (I). Ultrasonically clean and treat the sensor with bond-silane in preparation for packaging (II). Sand off supports and clean 3-D print in preparation for packaging (III). With a syringe and fine tip needle, draw a

border around the measurement chamber with liquid photoreactive resin. Place the sensor into the chamber and cure in place with a U-V flashlight (IV).

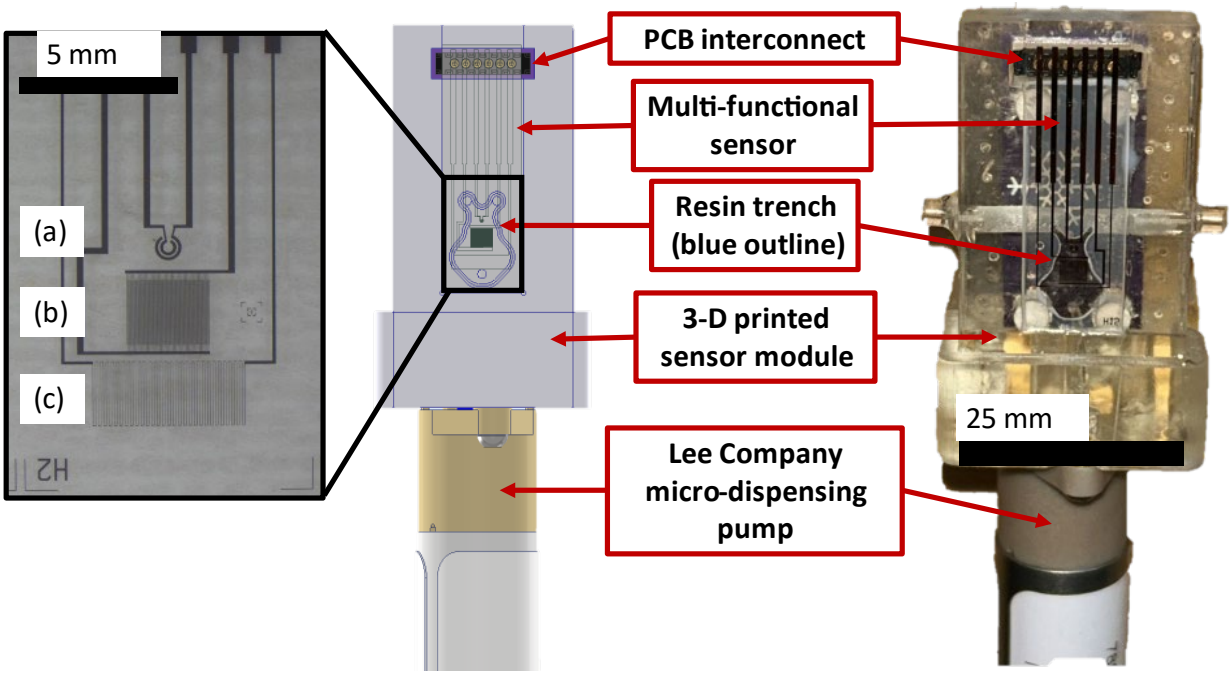

(a) - Electrical Conductivity Sensor

(b) - Interdigitated Electrode Array

(c) - Resistance Temperature Device

Figure 9: Multi-functional Sensor Module geometric layout. The MEMS device used for this research is shown to the left. This single chip has three sensing elements (a, b, c). The CAD model is shown in the middle with all components and features present. To the right is the implemented MSM under a UV light.

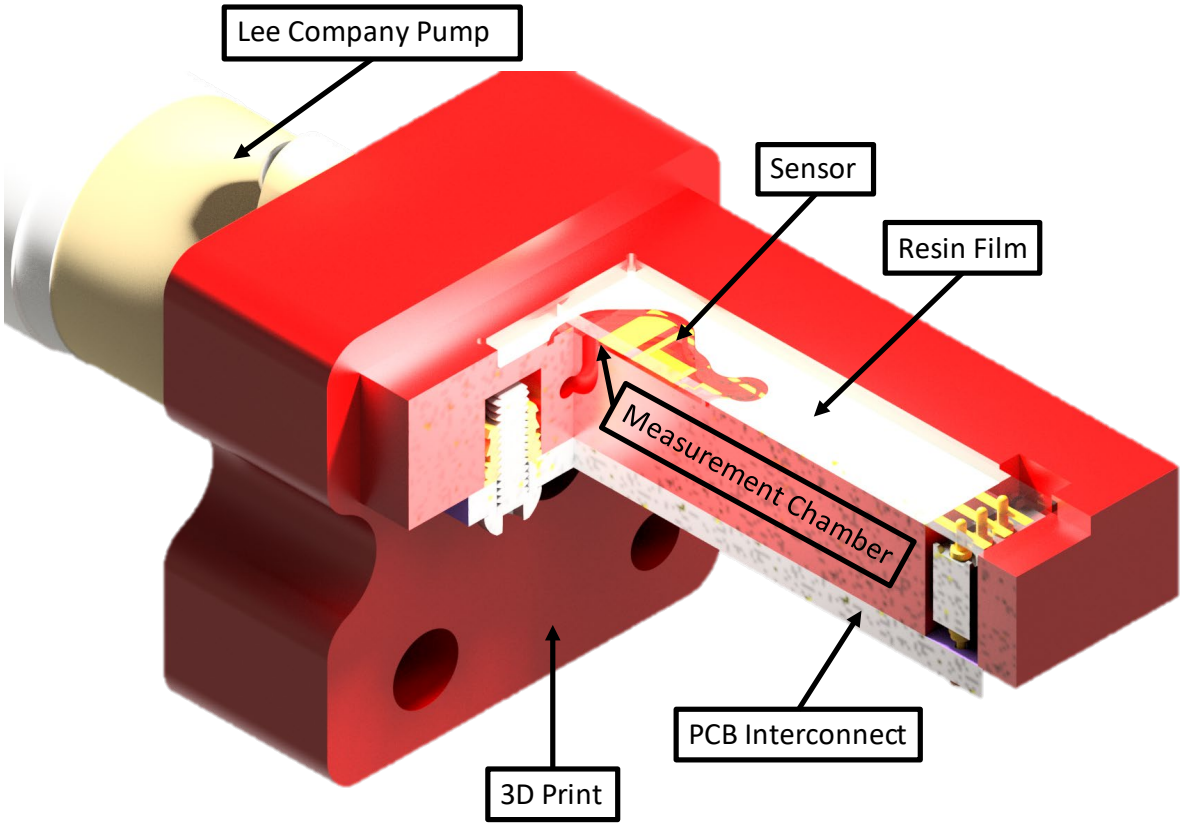

Figure 10: 3D cutaway of the MSM showing each component of a fully assembled multifunctional sensor module. The resin film (white) is a thin layer of cured 3D print material that adheres the sensor to the surface of the 3D printed part and provides an air-tight seal. This representation shows the details of how the sample enters the module and encounters the sensing elements. The gap between the 3D printed material (red) and the sensor surface is 300 µm.

Cleaning Solution Module

The MESA system has a 3D-printed reservoir and pump assembly called the cleaning solution module (CSM), containing 100 µS cm^{-1} conductivity solution (BIOPHRAM). The purpose of the CRM is to pump relatively low-conductivity water through the system's internal capillary network to purge the previous sample during the cleaning phase of the automation cycle. The CSM pump denoted P2 in Figure 5 is actuated for a set duration to transport cleaning solution into the SRM until the previously discussed level switch is triggered. Consequently, 100 µl of clean water is available for the MSM to transport through the measurement chamber and wash away any biological material or ions carried in the processed soil-water extract.

Figure 11: Cleaning Solution Module (CSM). A Lee Company micro-dispensing pump is mounted to the top of the reservoir containing 12 milliliters of 100 µS cm^{-1} conductivity solution.

MESA System: Assembly

The internal modules of the MEA system are assembled as a complete unit and then installed into an outdoor-rated acrylic shell (major dimensions 3.81 square x 53.3 cm). Stainless steel hardware with an O-ring seat head secures the probe internals to the exterior shell while preventing water ingress. Steel assembly pins were machined to size with small grooves to accept 1/16" "e" style retaining clips. The retaining clips provide position locating along the long axis of the MESA system. The assembly pins were press-fit into the base of the MSM and SRM to form the complete internal subassembly. Align the surface face of the MSM to the level switch wire side of the SRM. This shared face of the MESA internals must be aligned to side "C" of the MESA shell (see Appendix F). The control cables are routed to a battery-operated and rechargeable portable vacuum pump (Prenart) in addition to the custom PCB for controlling the electrical components. The automation code was created in the Arduino IDE (native language C/C++).

MESA System: Testing Procedures

Calibration

The electrical conductivity (EC) sensor shown in Figure 9 (a) was calibrated using a synthesized conductivity solution in a serial dilution series involving standardized conductivity solutions (BIOPHARM) and milli-Q deionized water (18.2 MΩcm). The solution series 100 (stock), 353, 706, 1413, 3220, and 6440 µS cm^{-1} were created by diluting stock solutions 1413 and 12,880 µS cm^{-1} with DI-water at whole number ratios. Calibration routines were performed by pipetting 100 µl of test solution from low to high strength into an inverted 3 ml syringe and cycling P1 at 5Hz until the test solution was covering the EC sensing elements with no visible

bubbles. Each solution in the series was evaluated three separate times using a HIOKI IM3536 LCR meter with a frequency sweep range of 1 kHz - 1 MHz at a potential of 10 mV, with DI rinsing between trials.

Packaging Experiment

EIS spectra were collected while exposing the EC sensor to 100 μS cm^{-1} standard solution (BIOPHARM) in three different states: untreated, after silane treatment, and fully packaged. The comparison of EIS spectra was used to determine if steps in the packaging test impact the electrochemical response of the EIS sensor when performing analyses. The sensor for this experiment was unused and ultrasonically cleaned in 95% isopropyl alcohol for 5 minutes, then dried with compressed air prior to experimentation. For the untreated and post silane treated states, the sensor was electronically connected to a card edge reader then 20 μl of test solution was pipetted onto the surface of the device. Three replicates of EIS spectra were collected with a HIOKI IM3536 LCR meter with a frequency sweep range of 1 kHz - 1 MHz, with DI rinsing between trials. Separately, the fully packaged EIS signatures were collected after P1 was used to transport the test solution into the measurement chamber. Three replicates of EIS spectra were collected with a HIOKI IM3536 LCR meter with a frequency sweep range of 1 kHz - 1 MHz at a potential of 10 mV, with DI rinsing between trials.

Cleaning Cycle Experiment

By design, the CSM must be about to hold enough cleaning solution to last for an entire growing season (May – October). To determine the correct amount of cleaning solution to allow, simulated and real experiments were conducted to study time and volume expense to physiochemically erase the previous sample. In both classes of experimentation, a solution with

strength of 1413 μS cm^{-1} (BIOPHARM) was primed in the measurement chamber. Then, cleaning solution with strength 100 μS cm^{-1} (BIOPHARM) was infused into the MSM while continuous conductivity measurements were collected.

COMSOL 6.0 was used to evaluate the transient chemical response within the measurement chamber during the cleaning process. The CAD Import Module was used to import the relevant geometry with high fidelity as shown in Figure 12 (a). The mesh size of ultra-fine shown in Figure 12 (b) was used to define the finite element analysis space for solving the governing equations.

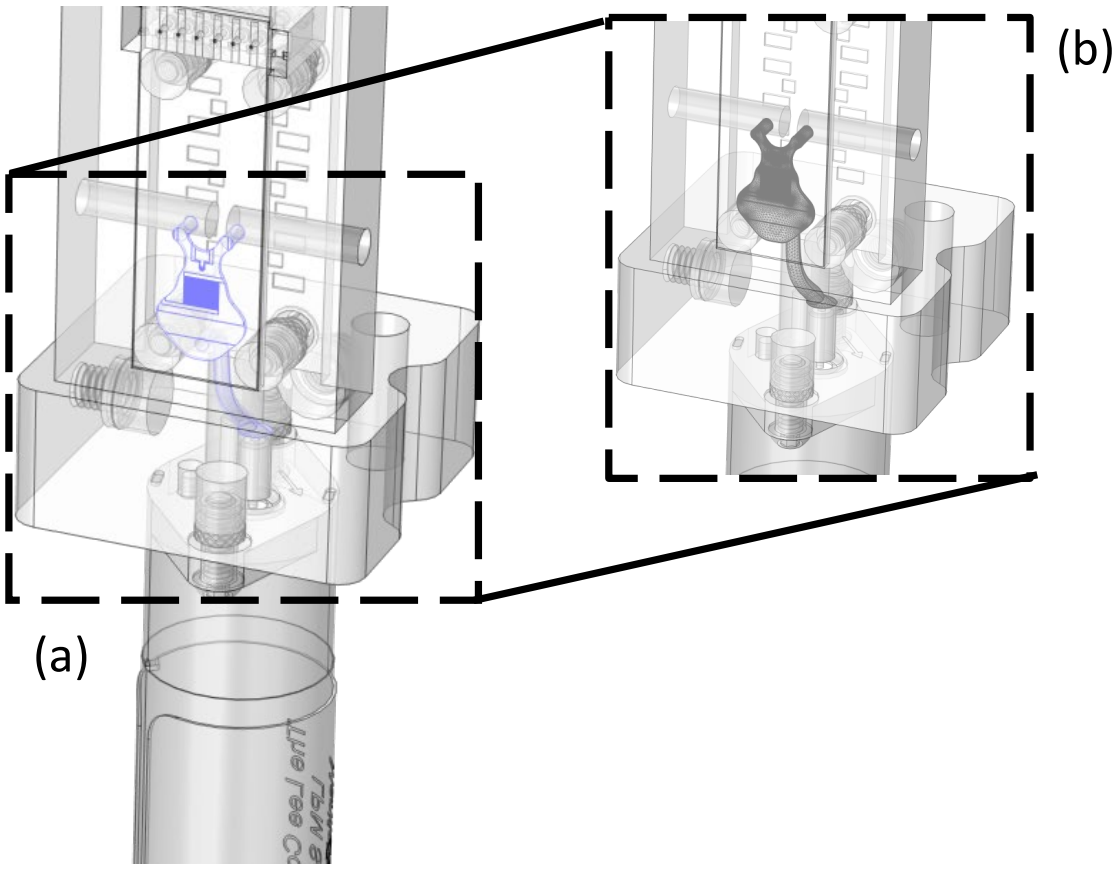

Figure 12: Imported geometry of the MSM and highlight solution space (a). Constructed computational mesh. Ultra-fine tetrahedral mesh calibrated for fluid mechanics was used (b).

The COMSOL simulation couples the Navier-Stokes momentum equations for incompressible fluids (Equation 4 and 5) with convection diffusion Equations (6 and 7) to determine the velocity, pressure, and conductivity throughout the simulation space at each time point. In this case, the solution parameters were recorded at the observational point probe located 50 μm from the surface of the conductivity sensor every 0.1 seconds throughout the simulation duration (1.5 seconds)

$$\rho \frac{\partial \boldsymbol{u}}{\partial t} + \rho(\boldsymbol{u} \cdot \nabla)\boldsymbol{u} = \nabla \cdot [-p + \boldsymbol{K}] + \boldsymbol{F} \quad (4)$$

$$\boldsymbol{\rho \nabla \cdot u} = 0 \quad (5)$$

$$\frac{\partial c_i}{\partial t} + \nabla \cdot \boldsymbol{J}_i + \boldsymbol{u} \cdot \nabla \mathrm{c}_i = R_i \quad (6)$$

$$\boldsymbol{J}_i = -D_{\boldsymbol{i}} \nabla c_i \quad (7)$$

In the equations above ρ is the fluid density (1000 g/l for water), u is the fluid velocity, p is the pressure, is the K accounts for internal stresses due to viscous effects, F accounts for external forces such as gravity, c_i is the chemical concentration, D_i is the diffusion coefficient (0.0016 mm^2 cm^{-1} for water), and R_i accounts for sources and sinks from internal chemical reactions ($R_i = 0$ for this simulation). These variables were chosen to reflect the conventions used in the COMSOL software. For additional information regarding the boundary conditions, initial conditions, solving parameters, see Appendix D.

Emulated Field Experiment

Separate soil columns were constructed from modified rain gauges (4” diameter) and filled with 250 g of gravel to function as a free-flowing layer, followed by 1000 g of sand (QUIKRETE) with 4 mm holes drilled in the base to allow drainage. The MESA system

components were arranged as shown in Figure 13 to facilitate soil-water extraction, followed by immediate electrical conductivity determination. A porous cup lysimeter (PRENART SUPER QUARTZ Mini, Avg. pore size 2 μm) was buried in the soil profile with silica flour (PRENART) to increase hydraulic conductivity between the lysimeter and the soil pores. The soil columns were brought to field capacity separately with electrical conductivity (EC) of known magnitudes from low to high strength, 0 (DI-water), 644, 1288, and 2576 μS cm^{-1} (BIOPHARM). Field capacity refers to the soil moisture held by the soil pores after excess water has drained from the column by gravity [62]. Then, soil-water samples were extracted by applying 50 kPa with a digitally controlled vacuum pump (PRENART), transported to the SRM then pumped into the measurement chamber of the MSM for analysis (refer to Figure 5 for hydraulic schematic). Impedance measurements at the optimal analysis frequency were collected with a HIOKI IM3536 LCR for 30 seconds to improve measurement fidelity. Three replicate extractions with measurements were collected for each conductivity solution strength to infer the water's electrical conductivity due to interactions with the naturally occurring salts held by the sand in the soil column. It was hypothesized that the EC of the sand (σ_{sand}) would be equal to the EC strength of the solution (σ_{input}), subtracted from the EC reading by the MSM ($\sigma_{extract}$) which brought the soil to field capacity, as shown in Equation 8.

$$\sigma_{sand} = \sigma_{extract} - \sigma_{input} \tag{8}$$

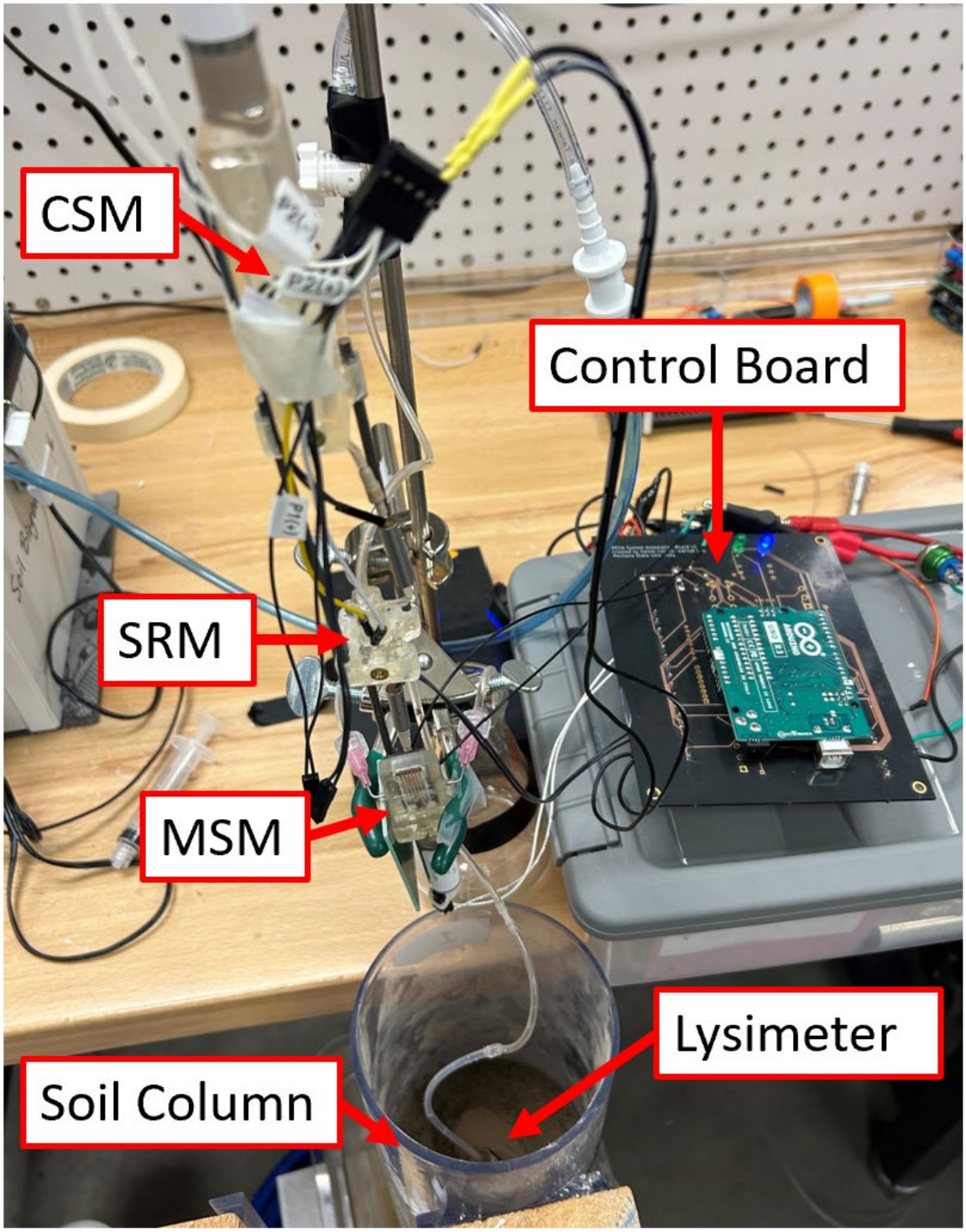

Figure 13: Complete MESA system. Probe layout and automation control board integration.

RESULTS & DISCUSSIONS

The following chapter presents results from calibrating the electrical conductivity sensor. Additionally, the results of a sample flushing experiment are presented with supporting computational fluid dynamic simulation results. Results of a packaging experiment reveal a key finding related to calibration procedures. Lastly, the results of an initial in-situ soil monitoring experiment are presented.

Electrical Conductivity Sensor

Best Analysis Frequency Determination

EIS measurements of six serial strength conductivity solutions ranging from 100 to 6440 $\mu S\ cm^{-1}$ provided sensor response data to be interpreted, as shown in Figure 14. Electrical conductivity (EC) measurements of bulk solution require a single analysis frequency which minimizes error and provides a linear relationship between impedance and the solution conductivity. The plot of real impedance shown below in Figure 14 was used to determine the ideal single-frequency analysis for EC measurements. Regions of the bode-real plot exhibit a constant Z_{real} response, which is independent of applied frequency across the entire tested conductivity range. Additionally, the Z_{real} measurement must have a linear relationship with the conductivity strength under test at a single frequency. As shown in Figure 15, EC measurement for 100 kHz provided the best fit ($R^2 = 0.992$), whereas 2, 30, and 70 kHz provided less goodness of fit ($R^2 = 0.645$, $R^2 = 0.977$, $R^2 = 0.991$, respectively). Lastly, the analysis frequency of 100 kHz is shown above ($R^2 = 0.992$). While 100 kHz provided the best fit, the standard deviation in the measurement using 100 kHz is larger than 70 kHz and therefore is not ideal. The

standard deviation of conductance when analyzing the 3220 μS cm^{-1} solution was 12.06 $\mu\Omega^{-1}$ and 11.29 $\mu\Omega^{-1}$ at 100 kHz and 70 kHz, respectively. In environmental research, soils with an EC of 1000 – 6000 μS cm^{-1} are common in agricultural settings [23], [55], [63]– [65] Reducing the measurement error within the operating range to optimize sensor function is paramount to the success of the MESA system. Thus, 70 kHz was chosen as the ideal analysis frequency.

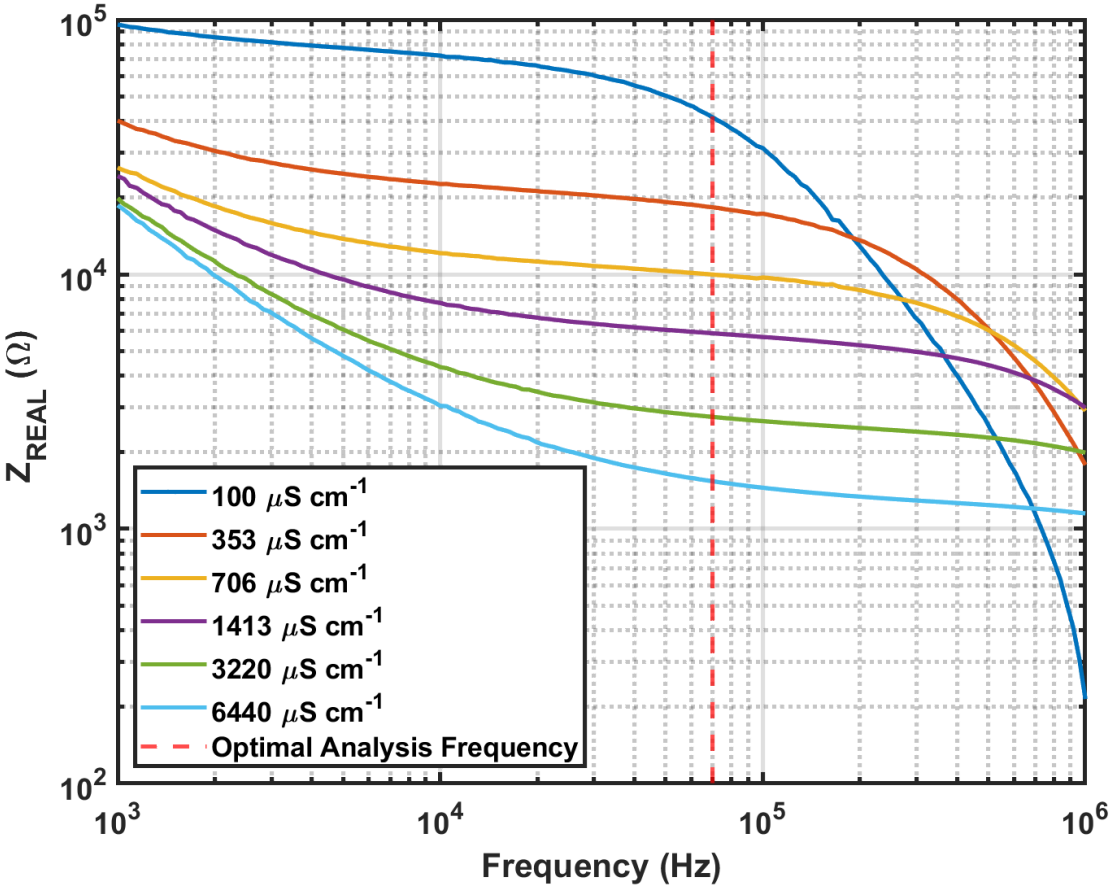

Figure 14: Plot of real impedance for six serial dilutions of stock electrical conductivity solution. The real portion of the impedance signature is plotted against the excitation frequency. The frequency was swept from 1 kHz to 1 MHz. The dashed red line indicates the ideal analysis frequency. This calibration is valid for only the individual sensor package used to create these data. Field use of the MSM requires correcting for temperature.

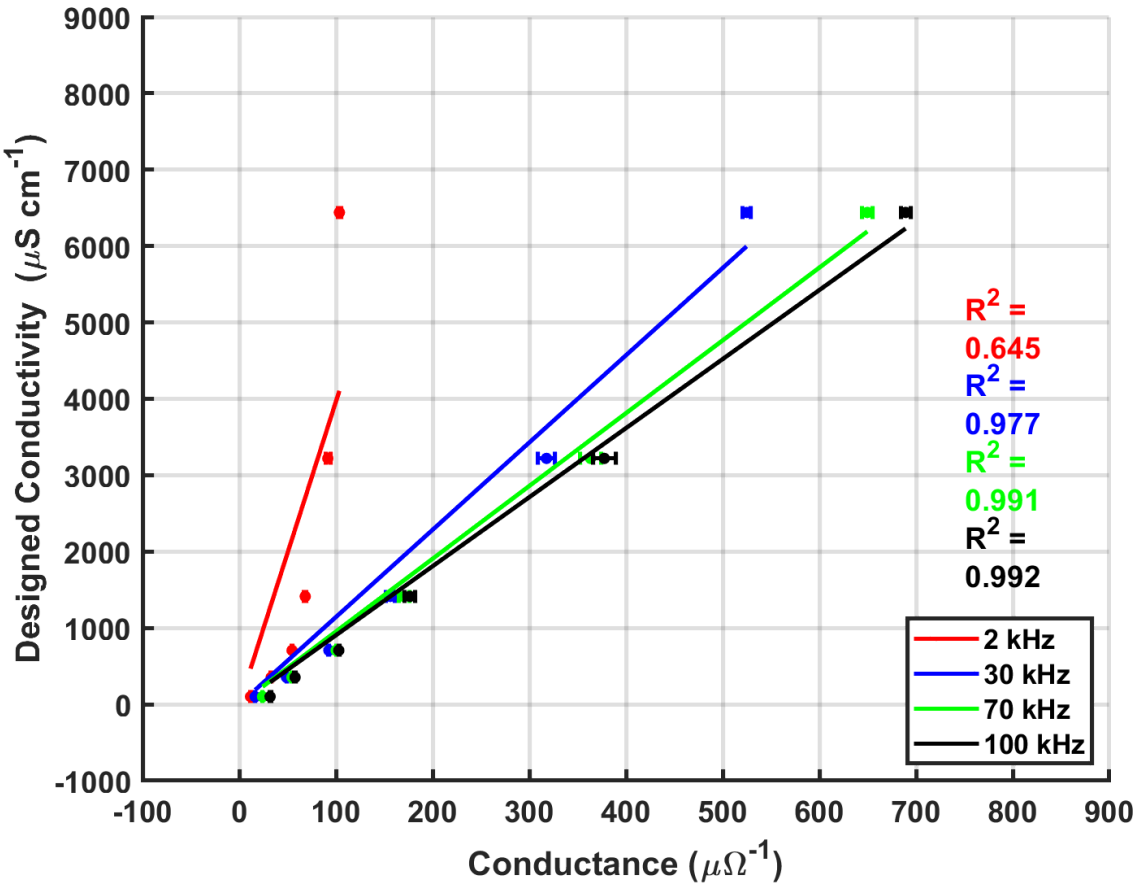

Figure 15: Calibration curves for comparing regression from analysis frequencies of 2, 30, 70, and 100 kHz. This calibration is valid for only the individual sensor package used to create these data. Field use of the MSM requires correcting for temperature.

Calibration

The EC sensor was calibrated using an analysis frequency of 70 kHz, and the cell constant k was found to be 9.530 cm^{-1} through the relationship between conductance and the EC, as shown in Figure 16. Electrical conductivity is temperature dependent; thus, it is critical to always measure the temperature of the fluid being measured. The electrical conductivity of ionic solution increases by approximately 2% per 1°C increase due to increases in kinetic energy leading to higher mobility [66]. Previous work by Neubauer *et al.* has outlined the equations that

may be used to normalize EC measurements to temperature for packaged micro-EC sensors [59]. In this calibration exercise, the real portion of impedance Z_{real} is taken to be the solution's bulk resistance. Electrical conductivity (EC) denoted σ is related to the conductance G linearly through the cell constant k as shown in Equation 9.

$$\sigma = kG \tag{9}$$

The calibration equation was obtained by substituting G with the inverse of Z_{real} and converting the resistance measured in ohms to micro-ohms, as shown in Equation 10.

$$\sigma\ (\mu S\ cm^{-1}) = k\left(\frac{10^6}{Z_{real,70\ kHz}}\right) \tag{10}$$

The calibration equation was used to compare the theoretical EC of the prepared test solution to the calculated EC by using Equation 10.

As shown in Figure 17, the calculated EC strongly agrees with the designed EC since the points reside near the line of slope 1. The calculated EC registers higher than the actual EC for the five lowest strength solutions evaluated. This result is acceptable because the estimates of EC in natural systems will be conservative and leave a beneficial margin of error.

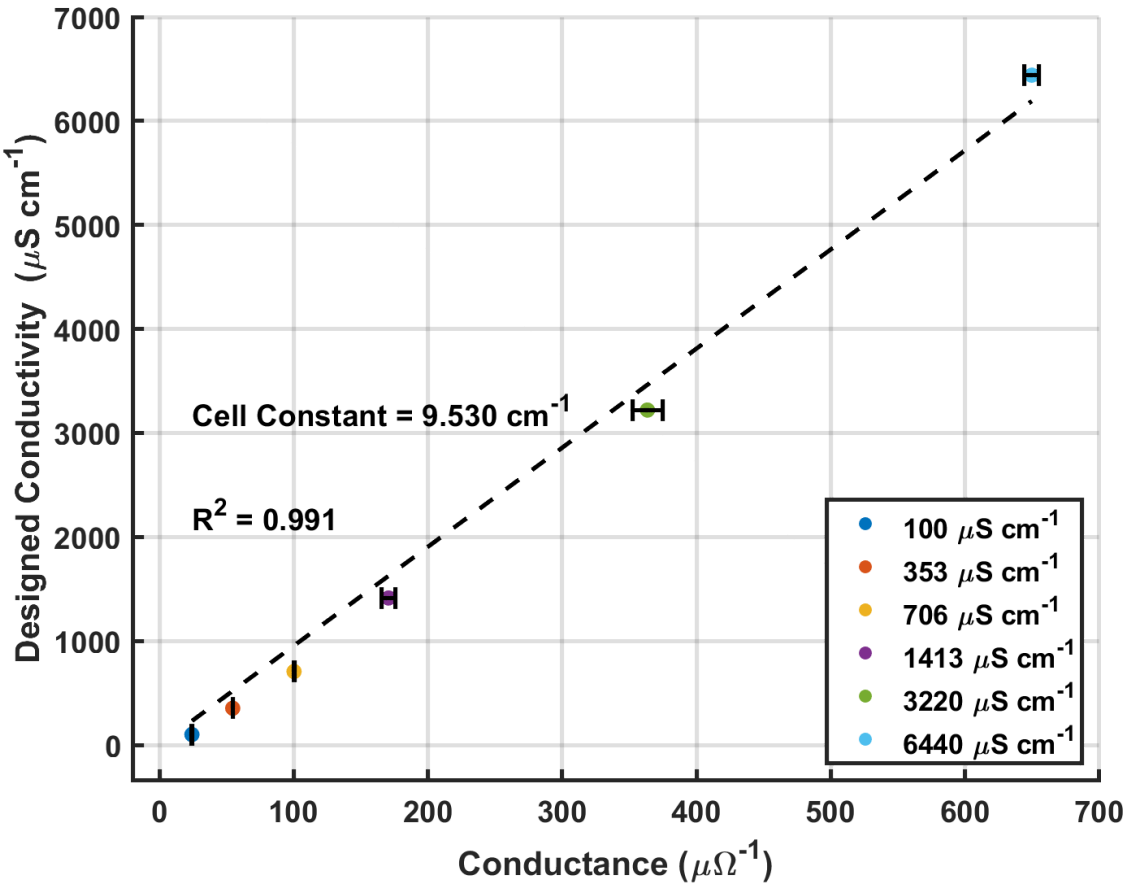

Figure 16: Electrical conductivity (EC) sensor calibration shows to have a cell constant 'k' of 9.530 with a strongly linear relationship (R^2 = 0.991). The range evaluated was 100 – 6440 µS cm^{-1}. This calibration is valid for only the individual sensor package used to create these data. Field use of the MSM requires correcting for temperature.

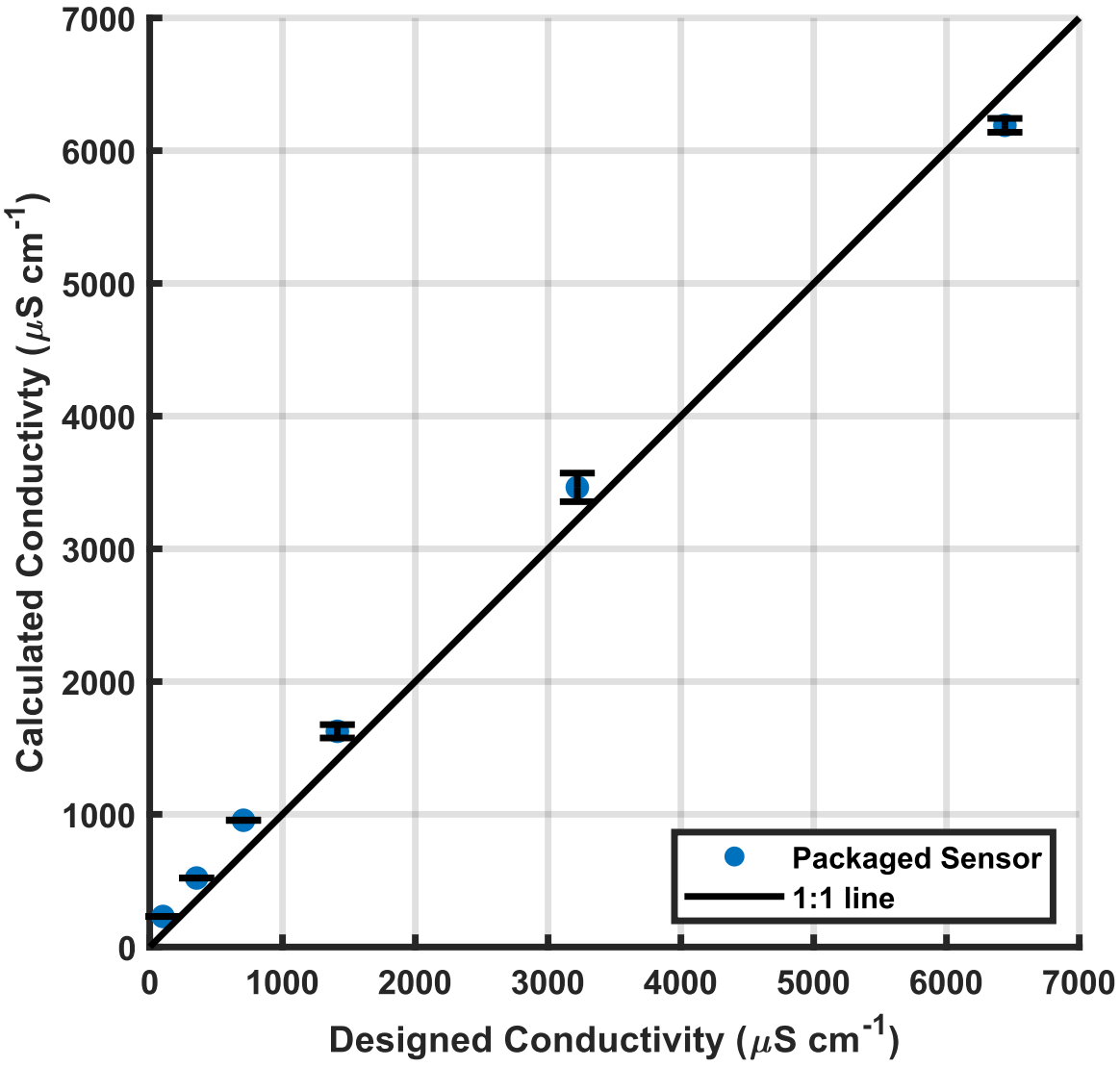

Figure 17: The calculated EC from the calibration equation yield results which strongly agree with the theoretical EC of the carefully produced test solutions. The vertical shift bias of the calibration is advantageous in environmental research. This calibration is valid for only the individual sensor package used to create these data. Field use of the MSM requires correcting for temperature.

Packaging Considerations

The multifunctional sensor module (MSM) must be calibrated in the packaged state because the sensor packaging procedure has been shown to modify the EIS signature compared to the original state. Nyquist plots for three sensor states in the packaging process are shown in Figure 18. The silane treatment procedure does not affect the chip's performance when tested with conductive solution; this finding is consistent with previous work [59]. Although, when the sensor is cured into place, there is a distinguishable change to the impedance signature when exposed to the same strength conductivity solution. The two stars in Figure 18 represent the points on each impedance signature at the 70 kHz level. There is a difference in solution resistance after packaging is completed at the same frequency. This phenomenon is likely due to electrical interactions between the sensing electrodes and the surrounding 3D print material. Thus, the sensor should be calibrated after the packaging process so that the cell constant can be accurate for that sensor and package combination.

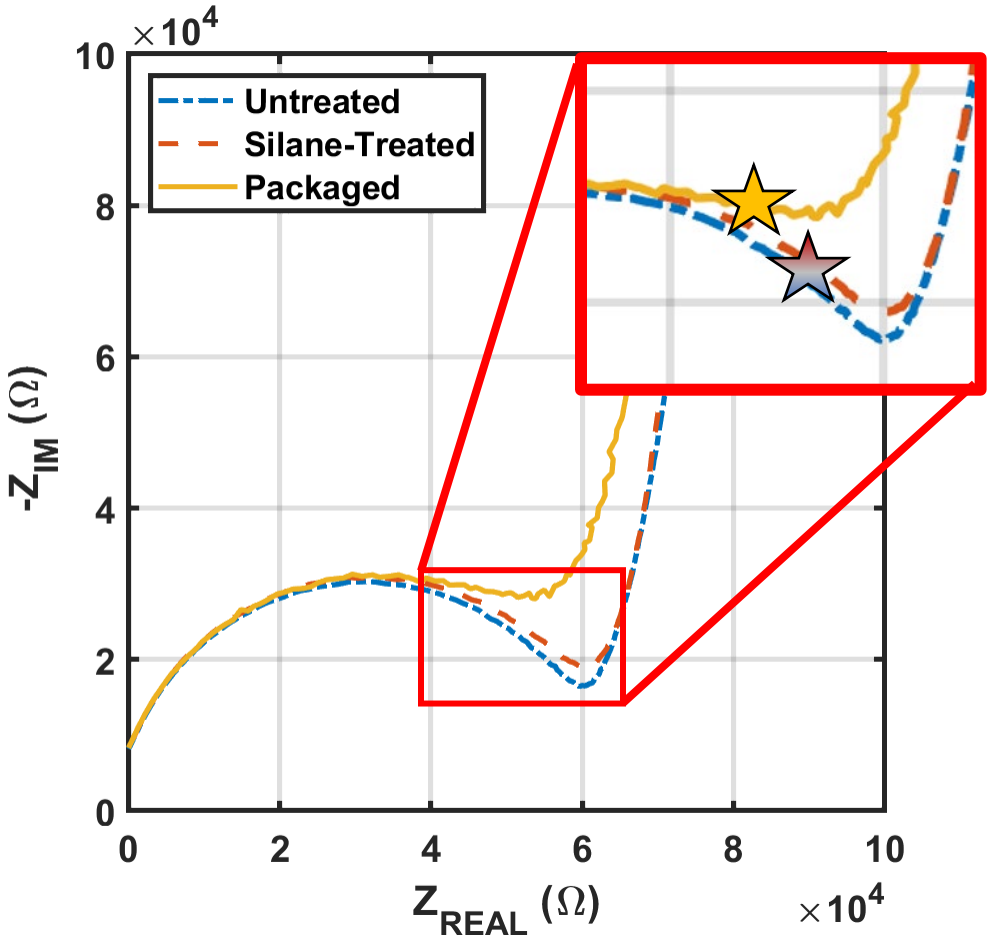

Figure 18: Nyquist signature of solution strength of 100 µS cm^{-1} for three sensor states present in the packaging process: untreated sensor (blue dashed), silane treated (red dashed), and the packaged sensor (solid gold). The gold star is shown to indicate the position on the Nyquist plot at the 70 kHz level for the packaged chip. The blue and red star shows the untreated and treated positions on the Nyquist plot at the 70 kHz level. The curves shown are the average result of three replicates.

The electrodes may interact with the surrounding PLA to introduce non-ideal equivalent circuit elements. Nyquist plot semicircular arc depressions or elevations are indicative of surface coating thickness variability, slow or uneven adsorption processes or nonuniform current distributions at the surface [46]. These findings indicate that the MSM must be calibrated in the packaged state for accurate performance.

Transient Cleaning Cycle Analysis

The flushing time required to clean out the MSM was found to be between 10 and 15 seconds by examining the sigmoid, as shown in Figure 19. These findings serve as programmatic guidance for the automation code. The time required for the signal to stabilize in this experiment is used to understand what volume of cleaning solution must be expended after each extraction and measurement process. P1 operates with an average flow rate of 50 µl s^{-1}. Multiplying the infusion rate by the time required to clean the MSM, the volume required to pass through the system is approximately 625 µl. For conservative estimates, the internal volume of the CSM was required to be greater than 4.8 ml such that the system can perform a system rinse twice for every measurement cycle (once per week). The CSM internal volume has been designed with a safety factor of 2.5 to ensure that there will be enough cleaning solution on board resulting in a target internal volume of 12 ml. There appears to be a horizontal time shift in the response curve between trials 1, 2, and 3. This is thought to be an artifact of the experimental process. Meaning, the time shift here is attributed to the delay between the targeted pump actuation instant and the time in which it was turned on. The decay rate between all three trials seems to be constant relative to each other. Additionally, the impedance reading during baseline reading (before turning the pump on) was much higher than the other trials. This problem was likely caused by a microbubble covering a portion of the electrode (this section of data has been omitted). However, the simulated cleaning cycle response shows a notable different result. The result of the COMSOL simulation response curve in Figure 20 suggests that within 0.8 seconds of pumping the cleaning solution into the measurement chamber, the conductivity of the solution in contact with the EC sensing electrode would be in equilibrium with the input concentration. In 0.8

seconds 40 µl will have been pumped through the measurement chamber, which has an internal volume of 27.8 µl. The experimental results do not agree with the theoretical results; this is quite unexpected. Other mechanisms must be affecting the rate at which the sensor can respond to the chemical changes. For example, the size of the electrical field extending into the sample solution must be much smaller than previously thought. The observational point probe defined in the simulation was positioned 50 µm into the solution space because it was previously thought that the electric field depth was equal to the sensor gap width. Considering that the fluid velocity in the measurement chamber is lowest at the boundary (no-slip) the fluid flowing across the sensor in short proximity to the electrode surface is moving much slower than the bulk fluid velocity. Perhaps the electrode is only interacting with fluid in this slow-moving regime thus lengthening the turnover time observed in the data shown in Figure 19.

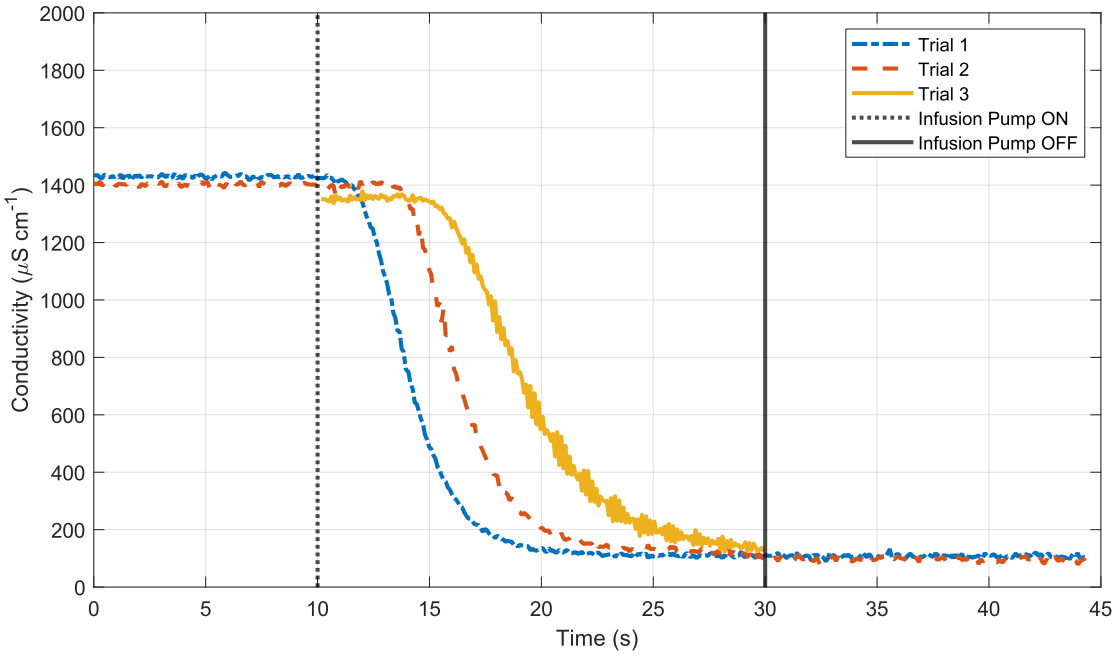

Figure 19: Continuous impedance measurements of the cleaning cycle.

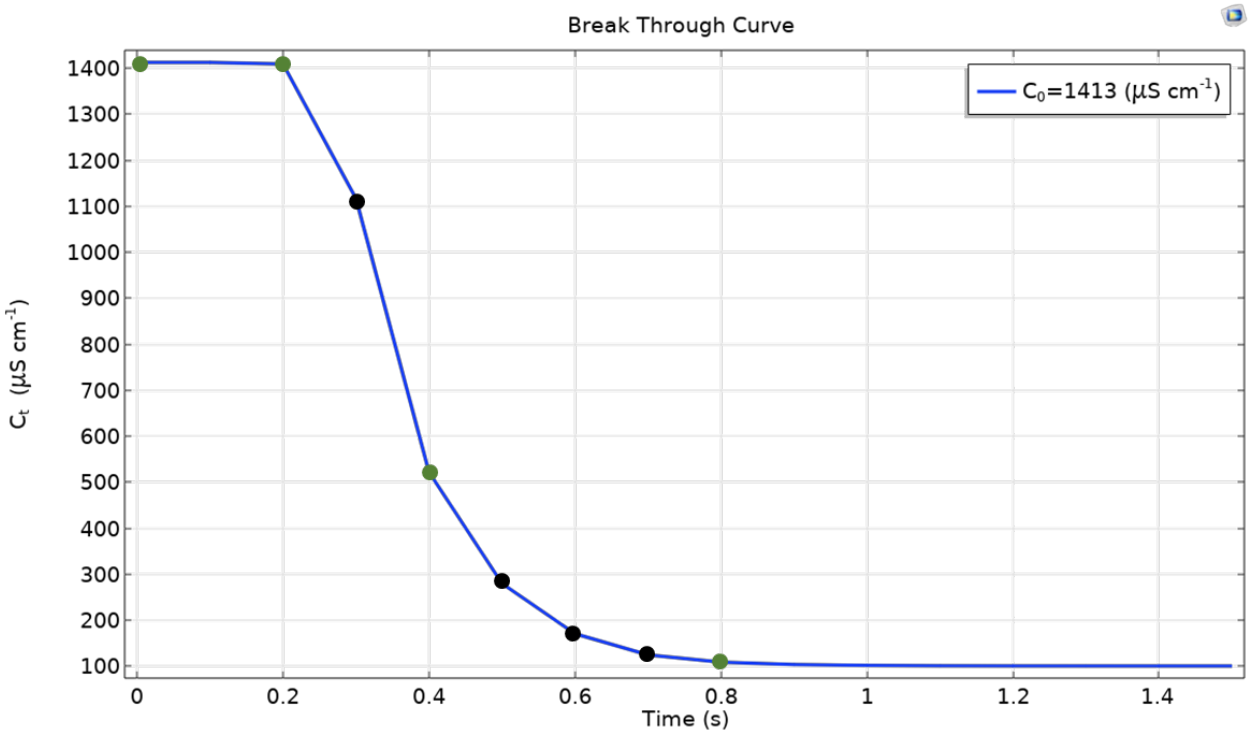

Figure 20: Transient theoretical result of the simulated cleaning cycle. Conductivity strength at the point probe was recorded every 0.1 seconds. The green dots represent time points when 3D visualizations are shown in Figure 21.

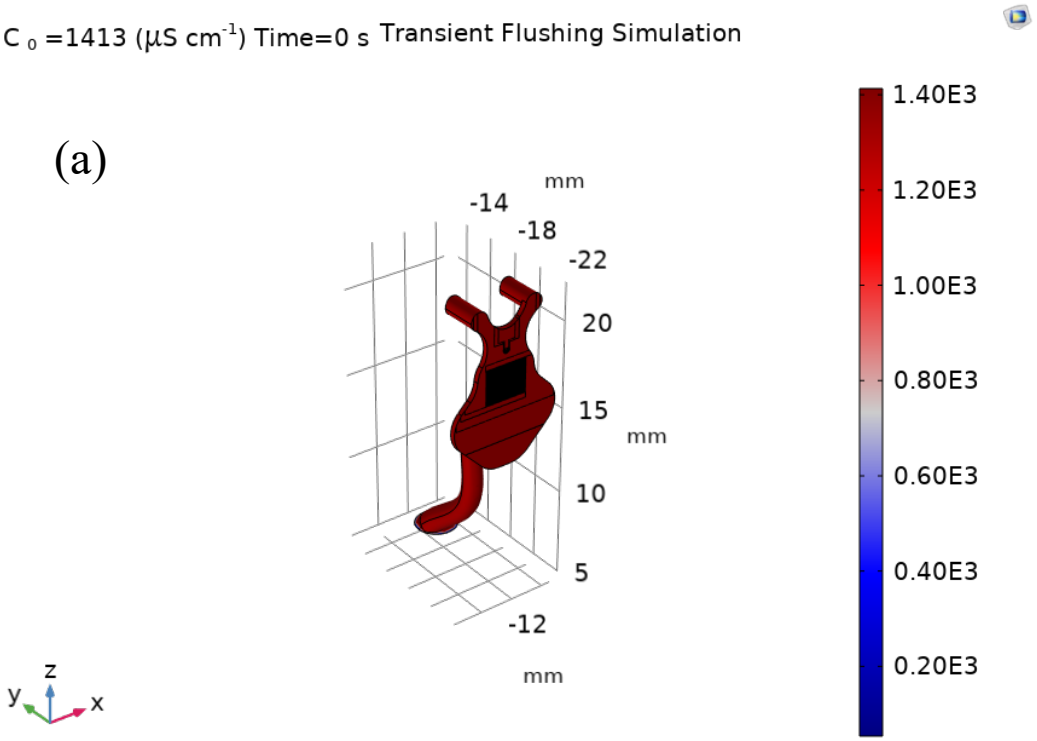
C 0 =1413 (μS cm-1) Time=0 s Transient Flushing Simulation
(a)
mm
-14
-18
-22
20
15
mm
10
5
-12
mm
z
y
x
1.40E3
1.20E3
1.00E3
0.80E3
0.60E3
0.40E3
0.20E3

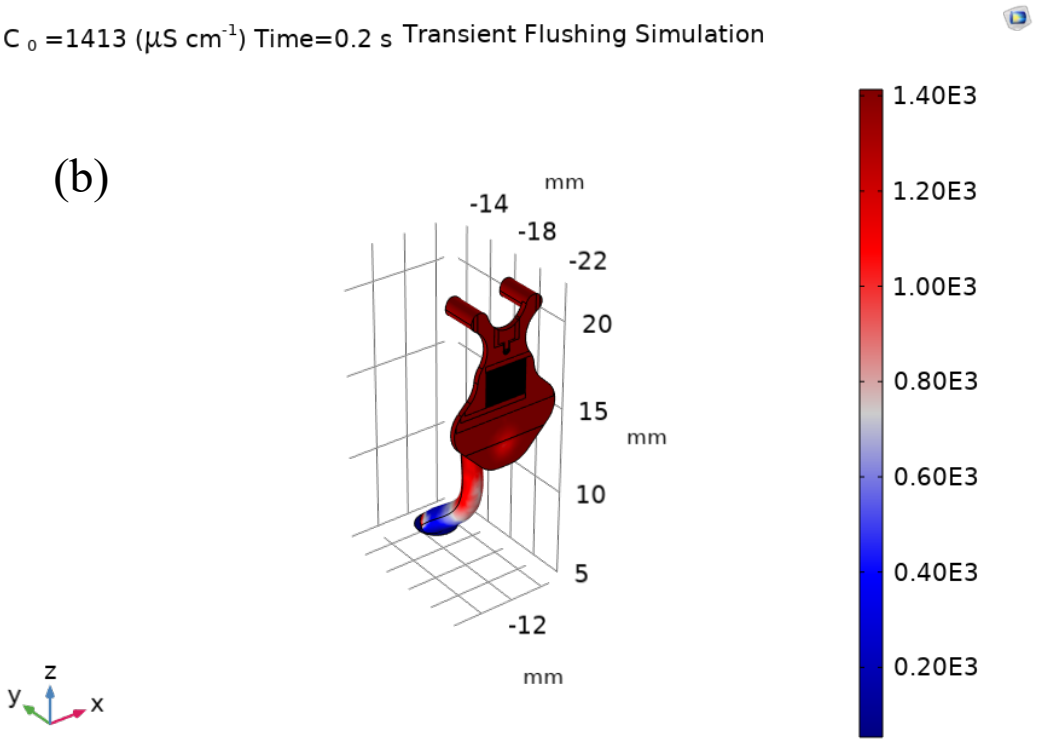
C 0 =1413 (μS cm-1) Time=0.2 s Transient Flushing Simulation
(b)
mm
-14
-18
-22
20
15
mm
10
5
-12
mm
z
y
x
1.40E3
1.20E3
1.00E3
0.80E3
0.60E3
0.40E3
0.20E3

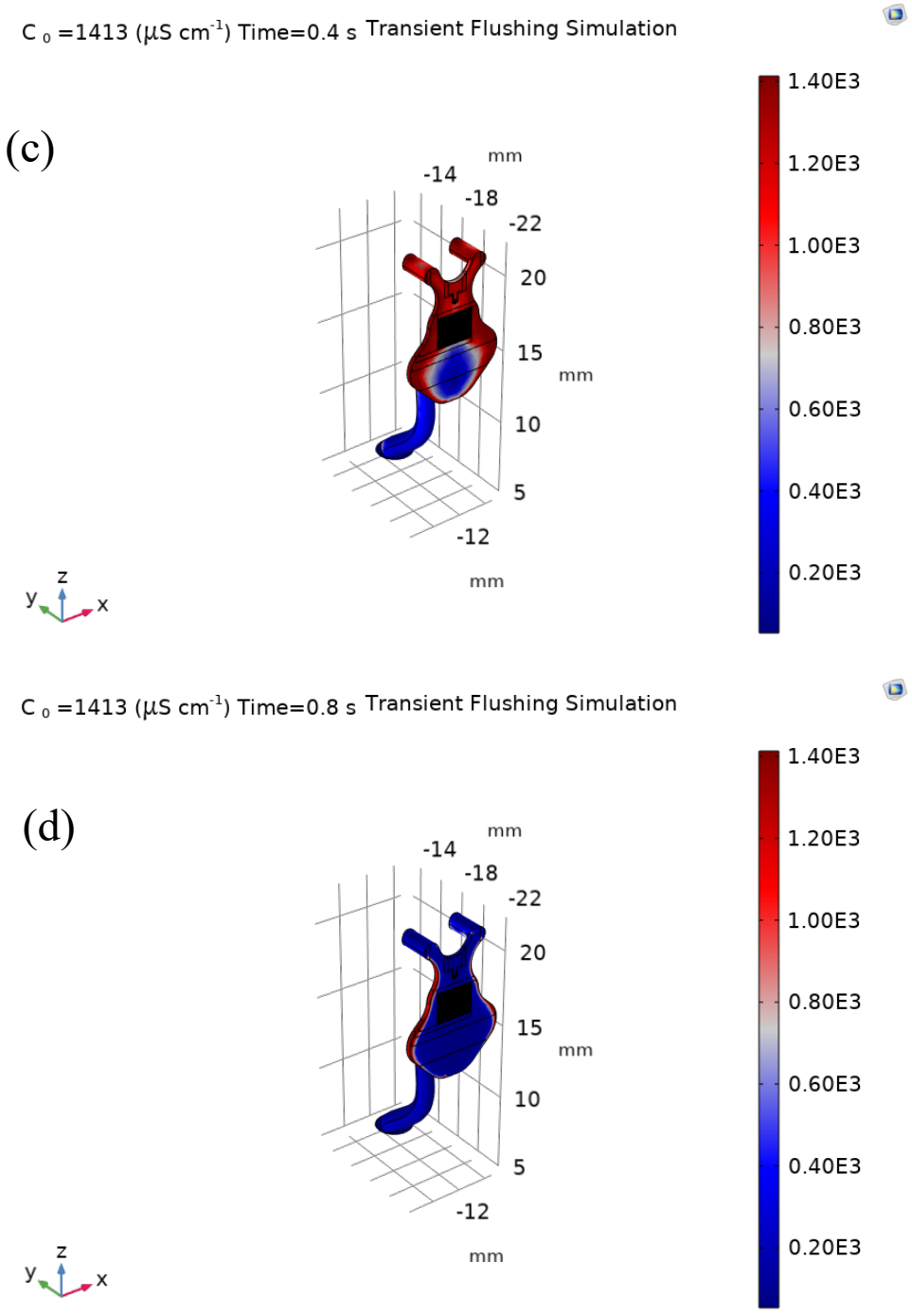

Figure 21: COMSOL 3-D color plot results from the start of the simulation until the steady state result. The initial concentration (C_0) strength in the domain is 1413 µS cm^{-1} (a). The strength of the cleaning solution being pumped in is 100 µS cm^{-1} in blue (b). After 0.4 seconds the cleaning solution has begun to enter the effected zone of the EC electrode (c). The measurement chamber is filled with cleaning solution (d).

Since considerable disagreement exists between the theoretical and experimental results regarding the cleaning cycle process, a feedback loop should be introduced. The loop would measure the EC of the solution throughout the cleaning process to determine exactly when the module is clean. The results of this experiment show that the EC sensor can acquire a stable signal when exposed to 100 $\mu S\ cm^{-1}$. Instead of prescribing P2 to run for a set duration, real-time signals could be used to trigger a stop cycle to P2 under the pretense that the sensor is reading a conductivity equal to 100 $\mu S\ cm^{-1} \pm 10\%$. With this logical feedback loop implemented, the system would be about to clean the sensor out and confirm that the sensor is clean in the same step.

Emulated Field Experiment

The MESA system has proved to be a promising tool for rapidly analyzing soil-water samples by automated, *in-situ* extraction and analysis. Single-frequency EIS measurements show that the electrical conductivity of MESA-extracted soil-water samples inherit ionic compounds from the sandy soil column. The increase in measured conductivity by the MESA system compared to the strength of the original input solution is derived from the salts present in the sand used for the soil column. The individual trial data show an increasing trend in all conductivity measurements from trials 1 to 3, as shown in Table 2. This suggests that the lysimeter had water within the pores from the previous column test that had been carried over and transported to the sensor at the beginning of the experiment involving the next highest strength solution. These results suggest that the first two extractions are likely to be inaccurate and should be discarded before recording actual data. This practice is consistent with standard

techniques [16]. Hence, the rightmost column in Table 2 shows the difference between the trial 3 reading and the conductivity strength of the input solution.

Table 2: Data from the emulated field test in µS cm^{-1}. These data are used to create Figure 22.

Input EC	Trial 1	Trial 2	Trial 3	Average	*T3 - input*
0 (DI water)	336	367	375	360	375
644	874	869	975	904	331
1288	1436	1556	1824	1590	536
2576	2065	2364	2862	2388	286

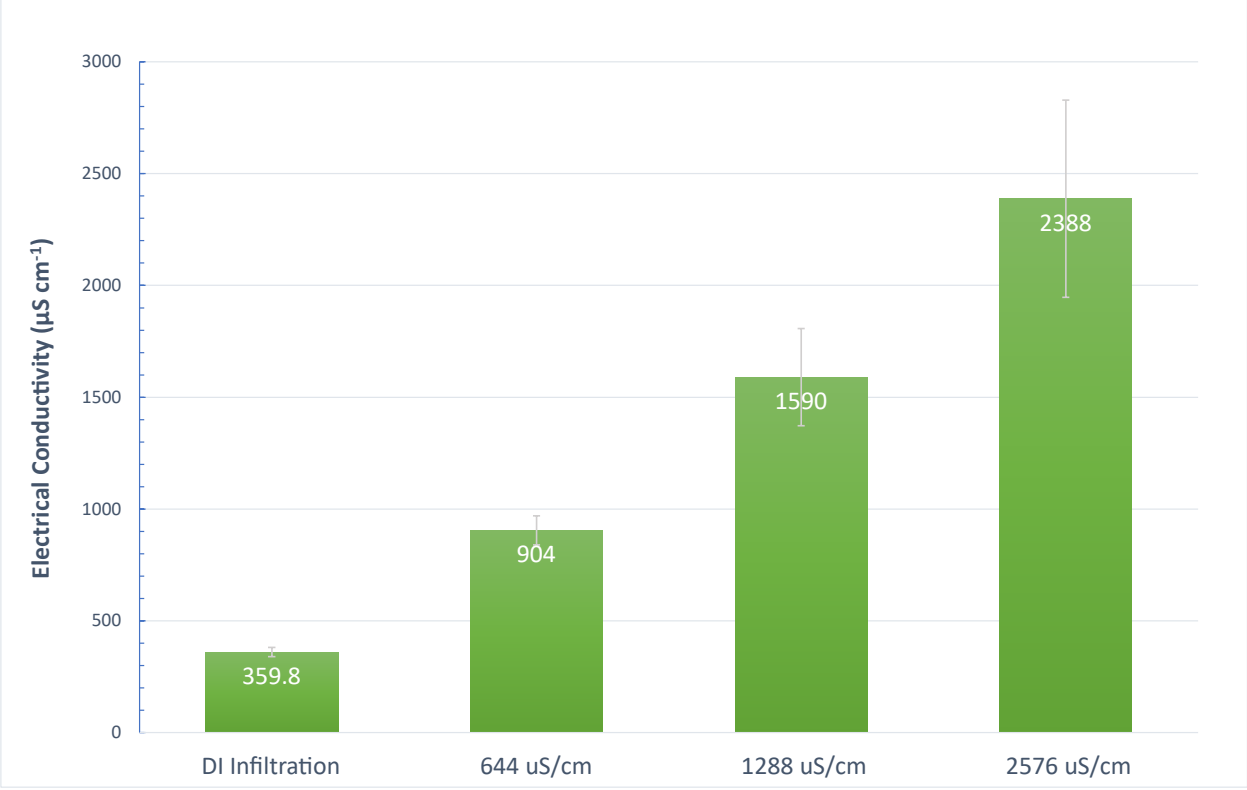

Figure 22: MESA system extraction and analysis of three soil columns at field capacity of known conductivity strengths (n=3). The x-axis represents the EC strength of the input solution to the soil column whereas the y-axis is the EC reading from the integrated sensor module (MSM).

To best estimate the electrical conductivity contributed by the ionic compounds coming from the sand, the average difference between trial 3 and the input strength was found to be 380 μS cm^{-1}.

CONCLUSION AND FUTURE OUTLOOK

Miniaturized sensors were integrated into a novel environmental monitoring tool. Packaging the EIS sensor into a 3D-printed module has shown to influence the cell constant and, therefore, must be calibrated in the post-packaged state. The electrical conductivity sensing electrodes have shown reproducible measurements of calibrated solutions across an applicable range for environmental research; however, EC measurements must be corrected for operating temperatures not equal to 25 °C. Automation of the MESA system has required the addition of micro-dispensing and valve control devices; thus, a programmable circuit board has been created to control all the fluid management devices. The MESA system has been used in a pseudo field experiment to test the efficacy of the system components and to determine the inherited electrical conductivity of test sand initially at field capacity.

The MESA system will be used in continued research activities in the Judith River Watershed to acquire new data from micro-samples processed by the automated probe. In the future, additional chemicals will be analyzed with the automated probe, like nitrate and pH levels. Thus, the next major improvement of the MESA system should be a modification of the integrated sensor by functionalizing the surface of the gold electrodes to be selective for target analytes. In addition to the EC sensor studied in this work, the other electrodes could be functionalized for pH and nitrate as outlined in the review of microsensor technologies for environmental monitoring, as shown in Figure 23. Automated extraction and chemical analysis of natural waters in semi-arid agricultural landscapes will enhance our understanding of biogeochemical processes within low-moisture soils' micropore structure. Lastly, real-time

measurements of compounds such as nitrate could provide producers insight into improving water quality in Montana.

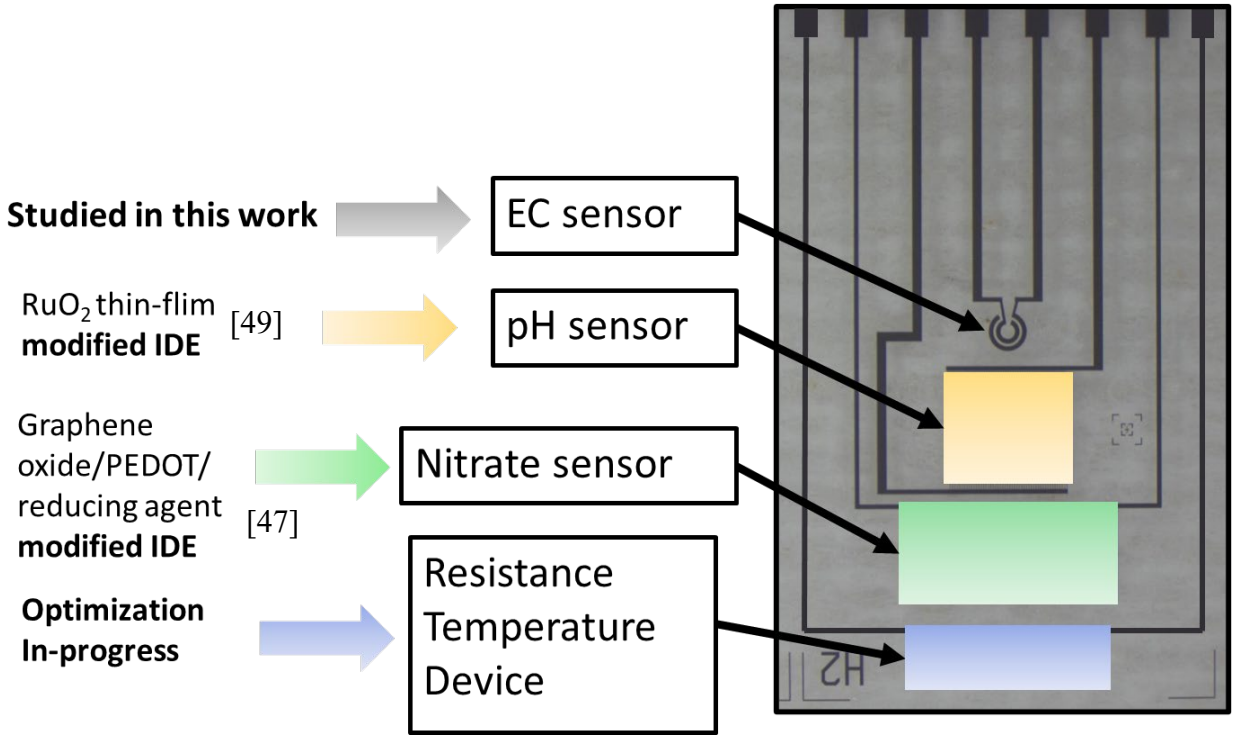

Figure 23: Proposed future sensor platform for in-situ environmental monitoring. The electrical conductivity sensor has been studied in this work and the optimization of the resistance temperature device is currently in progress. In the future, additional IDE structures could be modified to be sensitive to pH and NO_3^-.

REFERENCES CITED

[1] J. P. Bocquet-Appel, “When the world’s population took off: The springboard of the neolithic demographic transition,” *Science*, vol. 333, no. 6042. pp. 560–561, Jul. 29, 2011. doi: 10.1126/science.1208880.

[2] United Nations, “The World Population Prospects: 2015 Revision,” 2015. https://www.un.org/en/development/desa/publications/world-population-prospects-2015-revision.html (accessed Jan. 21, 2023).

[3] E. S. Bernhardt, E. J. Rosi, and M. O. Gessner, “Synthetic chemicals as agents of global change,” *Front Ecol Environ*, vol. 15, no. 2, pp. 84–90, Mar. 2017, doi: 10.1002/fee.1450.

[4] W. Steffen *et al.*, “Planetary boundaries: Guiding human development on a changing planet,” *Science (1979)*, vol. 347, no. 6223, Feb. 2015, doi: 10.1126/science.1259855.

[5] F. Stuart. Chapin III, *Principles of Terrestrial Ecosystem Ecology*, 2nd ed. 2011. New York, NY: Springer New York, 2011.

[6] M. Le Moal *et al.*, “Eutrophication: A new wine in an old bottle?,” *Science of the Total Environment*, vol. 651. Elsevier B.V., pp. 1–11, Feb. 15, 2019. doi: 10.1016/j.scitotenv.2018.09.139.

[7] W. De Vries, J. Kros, C. Kroeze, and S. P. Seitzinger, “Assessing planetary and regional nitrogen boundaries related to food security and adverse environmental impacts,” *Current Opinion in Environmental Sustainability*, vol. 5, no. 3–4. pp. 392–402, Sep. 2013. doi: 10.1016/j.cosust.2013.07.004.

[8] S. Singh *et al.*, “Nitrates in the environment: A critical review of their distribution, sensing techniques, ecological effects and remediation,” *Chemosphere*, vol. 287. Elsevier Ltd, Jan. 01, 2022. doi: 10.1016/j.chemosphere.2021.131996.

[9] S. Shukla and A. Saxena, “Global Status of Nitrate Contamination in Groundwater: Its Occurrence, Health Impacts, and Mitigation Measures,” in *Handbook of Environmental Materials Management*, Springer International Publishing, 2019, pp. 869–888. doi: 10.1007/978-3-319-73645-7_20.

[10] F. Serio *et al.*, “Groundwater nitrate contamination and agricultural land use: A grey water footprint perspective in Southern Apulia Region (Italy),” *Science of the Total Environment*, vol. 645, pp. 1425–1431, Dec. 2018, doi: 10.1016/j.scitotenv.2018.07.241.

[11] H. M. Rizeei, O. S. Azeez, B. Pradhan, and H. H. Khamees, “Assessment of groundwater nitrate contamination hazard in a semi-arid region by using integrated parametric IPNOA and data-driven logistic regression models,” *Environ Monit Assess*, vol. 190, no. 11, Nov. 2018, doi: 10.1007/s10661-018-7013-8.

[12] USDA, “2017 USDA CENSUS OF AGRICULTURE,” 2017. [Online]. Available: www.nass.usda.gov/go/cropnames.pdf.

[13] University of Montana and Montana State Library, “Relative Effective Annual Precipitation (REAP) data for Montana ,” 2019. https://www.arcgis.com/home/item.html?id=57e71c87fa284ff49f17bfaf74fe24f1 (accessed Mar. 30, 2023).

[14] USDA, “USDA Wheat Census Data ,” 2017. https://www.arcgis.com/home/item.html?id=070ce5f4390c4be4b077ab88820052a7 (accessed Mar. 30, 2023).

[15] W. A. Sigler, S. A. Ewing, C. A. Jones, R. A. Payn, P. Miller, and M. Maneta, “Water and nitrate loss from dryland agricultural soils is controlled by management, soils, and weather,” *Agric Ecosyst Environ*, vol. 304, Dec. 2020, doi: 10.1016/j.agee.2020.107158.

[16] Neal. Wilson, *Soil water and ground water sampling* . Boca Raton, Fla: Lewis Publishers, 1995.

[17] A. Reck, E. Paton, and B. Kluge, “Advanced In Situ Soil Water Sampling System for Monitoring Solute Fluxes in the Vadose Zone,” *Vadose Zone Journal*, vol. 18, no. 1, pp. 1–8, Jan. 2019, doi: 10.2136/vzj2019.01.0008.

[18] C. Z. Lai, M. D. DeGrandpre, and R. C. Darlington, “Autonomous optofluidic chemical analyzers for marine applications: Insights from the Submersible Autonomous Moored Instruments (SAMI) for pH and pCO2,” *Front Mar Sci*, vol. 4, no. JAN, Jan. 2018, doi: 10.3389/fmars.2017.00438.

[19] A. D. Beaton *et al.*, “Lab-on-Chip Measurement of Nitrate and Nitrite for In Situ Analysis of Natural Waters,” *Environ. Sci. Technol*, vol. 46, 2012, doi: 10.1021/es300419u.

[20] F. Wang *et al.*, “Lab on a Chip Rapid nitrate determination with a portable lab-on-chip device based on double microstructured assisted reactors †,” vol. 21, p. 1109, 2021, doi: 10.1039/d0lc01057j.

[21] M. Smolka *et al.*, “A mobile lab-on-a-chip device for on-site soil nutrient analysis,” *Precis Agric*, vol. 18, pp. 152–168, 2017, doi: 10.1007/s11119-016-9452-y.

[22] D. Jackson-Smith, S. Ewing, C. Jones, A. Sigler, and A. Armstrong, “The road less traveled: Assessing the impacts of farmer and stakeholder participation in groundwater nitrate pollution research,” *J Soil Water Conserv*, vol. 73, no. 6, pp. 610–622, Nov. 2018, doi: 10.2489/jswc.73.6.610.

[23] Ranbir. Chhabra, *Soil salinity and water quality* . Rotterdam ; Balkema, 1996.

[24] W. Schlesinger and E. Bernhardt, *Biogeochemistry: An Analysis of Global Change*, 4th ed. Candice Janco, 2022.

[25] C. Jones, R. Engel, and K. Olson-Rutz, "Soil acidification in the semiarid regions of North America's Great Plains," *Crops & Soils*, vol. 52, no. 2, pp. 28–56, Mar. 2019, doi: 10.2134/cs2019.52.0211.

[26] Environmental Protection Agency, "National Primary Drinking Water Regulations," 2009.

[27] J. Schullehner, B. Hansen, M. Thygesen, C. B. Pedersen, and T. Sigsgaard, "Nitrate in drinking water and colorectal cancer risk: A nationwide population-based cohort study," *Int J Cancer*, vol. 143, no. 1, pp. 73–79, Jul. 2018, doi: 10.1002/ijc.31306.

[28] D. Majundar, "The Blue Baby Syndrome Nitrate Poisoning in Humans," 2003.

[29] WHO, "Methemoglobinemia," 2020.

[30] A. T. Jan, M. Azam, K. Siddiqui, A. Ali, I. Choi, and Q. M. R. Haq, "Heavy metals and human health: Mechanistic insight into toxicity and counter defense system of antioxidants," *International Journal of Molecular Sciences*, vol. 16, no. 12. MDPI AG, pp. 29592–29630, Dec. 10, 2015. doi: 10.3390/ijms161226183.

[31] R. Chakraborty, K. M. Khan, D. T. Dibaba, M. A. Khan, A. Ahmed, and M. Z. Islam, "Health implications of drinking water salinity in coastal areas of Bangladesh," *Int J Environ Res Public Health*, vol. 16, no. 19, Oct. 2019, doi: 10.3390/ijerph16193746.

[32] Peter Griess, "'Vorläufige Notiz über die Einwirkung von salpetriger Säure auf Amidinitro- und Aminitrophenylsäure,'" *Annalen der Chemie und Pharmacie*, vol. 106, pp. 123–125, 1858.

[33] M. Y. Kim and K. H. Lee, "Electrochemical Sensors for Sustainable Precision Agriculture—A Review," *Frontiers in Chemistry*, vol. 10. Frontiers Media S.A., May 09, 2022. doi: 10.3389/fchem.2022.848320.

[34] M. A. Ali *et al.*, "Continuous Monitoring of Soil Nitrate Using a Miniature Sensor with Poly(3-octyl-thiophene) and Molybdenum Disulfide Nanocomposite," *ACS Appl Mater Interfaces*, vol. 11, no. 32, pp. 29195–29206, 2019, doi: 10.1021/acsami.9b07120.

[35] M. Chen *et al.*, "An all-solid-state nitrate ion-selective electrode with nanohybrids composite films for in-situ soil nutrient monitoring," *Sensors (Switzerland)*, vol. 20, no. 8, Apr. 2020, doi: 10.3390/s20082270.

[36] K. Pietrzak, C. Wardak, and R. Łyszczek, “Solid Contact Nitrate Ion-selective Electrode Based on Cobalt(II) Complex with 4,7-Diphenyl-1,10-phenanthroline,” *Electroanalysis*, vol. 32, no. 4, pp. 724–731, Apr. 2020, doi: 10.1002/elan.201900462.

[37] S. S. M. Hassan, A. G. Eldin, A. E. G. E. Amr, M. A. Al-Omar, A. H. Kamel, and N. M. Khalifa, “Improved solid-contact nitrate ion selective electrodes based on multi-walled carbon nanotubes (MWCNTs) as an ion-to-electron transducer,” *Sensors (Switzerland)*, vol. 19, no. 18, Sep. 2019, doi: 10.3390/s19183891.

[38] K. Tsuchiya, T. Akatsuka, Y. Abe, and S. Komaba, “Design of all-solid-state chloride and nitrate ion-selective electrodes using anion insertion materials of electrodeposited poly(allylamine)-MnO2 composite,” *Electrochim Acta*, vol. 389, Sep. 2021, doi: 10.1016/j.electacta.2021.138749.

[39] V. A. T. , Dam and M. A. G. Zevenbergen, *Low Cost Nitrate Sensor for Agricultural Applications*. 2019.

[40] S. Zhao, J. Tong, Y. Li, J. Sun, C. Bian, and S. Xia, “Palladium-gold modified ultramicro interdigital array electrode chip for nitrate detection in neutralwater,” *Micromachines (Basel)*, vol. 10, no. 4, Apr. 2019, doi: 10.3390/mi10040223.

[41] H. Bagheri, A. Hajian, M. Rezaei, and A. Shirzadmehr, “Composite of Cu metal nanoparticles-multiwall carbon nanotubes-reduced graphene oxide as a novel and high performance platform of the electrochemical sensor for simultaneous determination of nitrite and nitrate,” *J Hazard Mater*, vol. 324, pp. 762–772, Feb. 2017, doi: 10.1016/j.jhazmat.2016.11.055.

[42] R. Ahmad, T. Mahmoudi, M. S. Ahn, J. Y. Yoo, and Y. B. Hahn, “Fabrication of sensitive non-enzymatic nitrite sensor using silver-reduced graphene oxide nanocomposite,” *J Colloid Interface Sci*, vol. 516, pp. 67–75, Apr. 2018, doi: 10.1016/j.jcis.2018.01.052.

[43] K. Fajerwerg, V. Ynam, B. Chaudret, V. Garçon, D. Thouron, and M. Comtat, “An original nitrate sensor based on silver nanoparticles electrodeposited on a gold electrode,” *Electrochem commun*, vol. 12, no. 10, pp. 1439–1441, Oct. 2010, doi: 10.1016/j.elecom.2010.08.003.

[44] J. Hu, J. Sun, C. Bian, J. Tong, and X. Shanhong, “3D Dendritic Nanostructure of Silver-Array: Preparation, Growth Mechanism and Application in Nitrate Sensor,” *Electroanalysis*, vol. 25, no. 2, pp. 546–556, Feb. 2013, doi: 10.1002/elan.201200465.

[45] H. R. Lotfi Zadeh Zhad and R. Y. Lai, “Comparison of nanostructured silver-modified silver and carbon ultramicroelectrodes for electrochemical detection of nitrate,” *Anal Chim Acta*, vol. 892, pp. 153–159, Sep. 2015, doi: 10.1016/j.aca.2015.08.022.

[46] V. F. Lvovich, *Impedance spectroscopy applications to electrochemical and dielectric phenomena* . Hoboken, N.J: Wiley, 2012. Accessed: Dec. 21, 2022. [Online]. Available: https://ebookcentral.proquest.com/lib/montana/detail.action?pq-origsite=primo&docID=817407

[47] M. A. Ali *et al.*, "Microfluidic impedimetric sensor for soil nitrate detection using graphene oxide and conductive nanofibers enabled sensing interface," *Sens Actuators B Chem*, vol. 239, pp. 1289–1299, 2017, doi: 10.1016/j.snb.2016.09.101.

[48] G. Yang, K. L. Kampstra, and M. R. Abidian, "High-performance conducting polymer nanofiber biosensors for detection of biomolecules," *Advanced Materials*, vol. 26, no. 29, pp. 4954–4960, Aug. 2014, doi: 10.1002/adma.201400753.

[49] R. H. G. Mingels, S. Kalsi, Y. Cheong, and H. Morgan, "Iridium and Ruthenium oxide miniature pH sensors: Long-term performance," *Sens Actuators B Chem*, vol. 297, Oct. 2019, doi: 10.1016/j.snb.2019.126779.

[50] L. Manjakkal, E. Djurdjic, K. Cvejin, J. Kulawik, K. Zaraska, and D. Szwagierczak, "Electrochemical Impedance Spectroscopic Analysis of RuO<inf>2</inf> Based Thick Film pH Sensors," *Electrochim Acta*, vol. 168, pp. 246–255, Jun. 2015, doi: 10.1016/j.electacta.2015.04.048.

[51] M. Lotfi Choobbari, A. Jahanshahi, and M. Zare, "AUT Journal of Electrical Engineering Design and fabrication of a rapid conductometric pH sensor based on metal-oxide technology," vol. 52, no. 2, pp. 217–222, 2020, doi: 10.22060/eej.2020.17982.5339.

[52] A. Adhikary, J. Roy, A. G. Kumar, S. Banerjee, and K. Biswas, "An Impedimetric Cu-Polymer Sensor-Based Conductivity Meter for Precision Agriculture and Aquaculture Applications," *IEEE Sens J*, vol. 19, no. 24, pp. 12087–12095, Dec. 2019, doi: 10.1109/JSEN.2019.2940159.

[53] W.-C. Lin, K. Brondum, C. W. Monroe, and M. A. Burns, "Multifunctional Water Sensors for pH, ORP, and Conductivity Using Only Microfabricated Platinum Electrodes," 2017, doi: 10.3390/s17071655.

[54] G. J. A. M. Brom-Verheijden, M. H. Goedbloed, and M. A. G. Zevenbergen, "A Microfabricated 4-Electrode Conductivity Sensor with Enhanced Range †," *Proc West Mark Ed Assoc Conf*, vol. 2, p. 797, 2018, doi: 10.3390/proceedings2130797.

[55] M. Lech *et al.*, "Monitoring of total dissolved solids on agricultural lands using electrical conductivity measurements," *Appl Ecol Environ Res*, vol. 14, no. 4, pp. 285–295, 2016, doi: 10.15666/aeer/1404_285295.

[56] Y. A. Vélez Justiniano *et al.*, “Mitigation and use of biofilms in space for the benefit of human space exploration,” *Biofilm*, vol. 5, Dec. 2023, doi: 10.1016/j.bioflm.2022.100102.

[57] M. McGlennen, M. Neubauer, M. Driesler, M. Dieser, C. M. Foreman, and S. Warnat, “Microsensors in Icy Environments to Detect Microbial Activities,” *Journal of Microelectromechanical Systems*, vol. 29, no. 5, pp. 853–859, Oct. 2020, doi: 10.1109/JMEMS.2020.3012420.

[58] M. Mcglennen, M. Dieser, C. M. Foreman, and S. Warnat, “Using Electrochemical Impedance Spectroscopy 2 to Study Biofilm Growth in a 3D-Printed Flow Cell System Montana State University.” [Online]. Available: https://ssrn.com/abstract=4309591

[59] M. Neubauer, M. McGlennen, S. Thomas, and S. Warnat, “3D printing on glass for direct sensor integration,” *Engineering Research Express*, vol. 1, no. 2, 2019, doi: 10.1088/2631-8695/ab5e9f.

[60] I. Pereiro, A. Fomitcheva Khartchenko, L. Petrini, and G. V. Kaigala, “Nip the bubble in the bud: A guide to avoid gas nucleation in microfluidics,” *Lab on a Chip*, vol. 19, no. 14. Royal Society of Chemistry, pp. 2296–2314, Jul. 21, 2019. doi: 10.1039/c9lc00211a.

[61] M. J. Männel, N. Weigel, N. Hauck, T. Heida, and J. Thiele, “Combining Hydrophilic and Hydrophobic Materials in 3D Printing for Fabricating Microfluidic Devices with Spatial Wettability,” *Adv Mater Technol*, vol. 6, no. 9, Sep. 2021, doi: 10.1002/admt.202100094.

[62] O. W. Israelsen and F. L. West, “Bulletin No. 183 - Water-Holding Capacity of Irrigated Soils,” 1922. [Online]. Available: https://digitalcommons.usu.edu/uaes_bulletins/149

[63] K. Adhikari, D. R. Smith, H. Collins, C. Hajda, B. S. Acharya, and P. R. Owens, “Mapping Within-Field Soil Health Variations Using Apparent Electrical Conductivity, Topography, and Machine Learning,” *Agronomy*, vol. 12, no. 5, May 2022, doi: 10.3390/agronomy12051019.

[64] D. L. Corwin and S. M. Lesch, “Application of soil electrical conductivity to precision agriculture: Theory, principles, and guidelines,” in *Agronomy Journal*, American Society of Agronomy, 2003, pp. 455–471. doi: 10.2134/agronj2003.4550.

[65] M. Lech *et al.*, “Monitoring of total dissolved solids on agricultural lands using electrical conductivity measurements,” *Appl Ecol Environ Res*, vol. 14, no. 4, pp. 285–295, 2016, doi: 10.15666/aeer/1404_285295.

[66] Electricity - Magnetism, “How does the electrical conductivity of liquids change with concentration and temperature?,” 2023. https://www.electricity-magnetism.org/how-does-the-electrical-conductivity-of-liquids-change-with-concentration-and-temperature/#:~:text=As%20the%20temperature%20of%20a%20solution%20increases%2

C%20the,between%20temperature%20and%20conductivity%20for%20most%20electrolyte%20solutions. (accessed Apr. 26, 2023).

[67] T. B. Pham, H. Bui, H. T. Le, and V. H. Pham, “Characteristics of the fiber laser sensor system based on etched-bragg grating sensing probe for determination of the low nitrate concentration in water,” *Sensors (Switzerland)*, vol. 17, no. 1, Jan. 2017, doi: 10.3390/s17010007.

[68] W. Ren, S. Mura, and J. M. K. Irudayaraj, “Modified graphene oxide sensors for ultra-sensitive detection of nitrate ions in water,” *Talanta*, vol. 143, pp. 234–239, Jun. 2015, doi: 10.1016/j.talanta.2015.05.073.

[69] F. Akhter, H. R. Siddiquei, M. E. E. Alahi, and S. C. Mukhopadhyay, “An IoT-enabled portable sensing system with MWCNTs/PDMS sensor for nitrate detection in water,” *Measurement (Lond)*, vol. 178, Jun. 2021, doi: 10.1016/j.measurement.2021.109424.

APPENDICES

APPENDIX A

AUTOMATION BOARD: HEAT GENERATION

Thermal imaging of the automation control board has proved that heat generation by the MOSFET controlling the vacuum pump will not be a safety hazard in field use. In general, consumer electronics begin to encounter heat-induced failures above 100 °C (212 °F). The NPN transistor used to switch on the system vacuum (MJH11022, onsemi) has an operating temperature range of -65 °C – 150 °C. The infrared images (FLUKE, TiS20) in Figure A1 show that the energized transistor reached a maximum temperature of 36 °C after 5 minutes of running the pump under full load (0.6 A). There are many other transistors and ICs on the MESA automation board; however, the others control devices with low power demands, so heat generation due to those devices will also not be an issue.

As a safety precaution, an auxiliary temperature sensor could be installed inside the enclosure with an emergency shutdown protocol that triggers if the temperature reading exceeds 90 °C for more than 60 seconds.

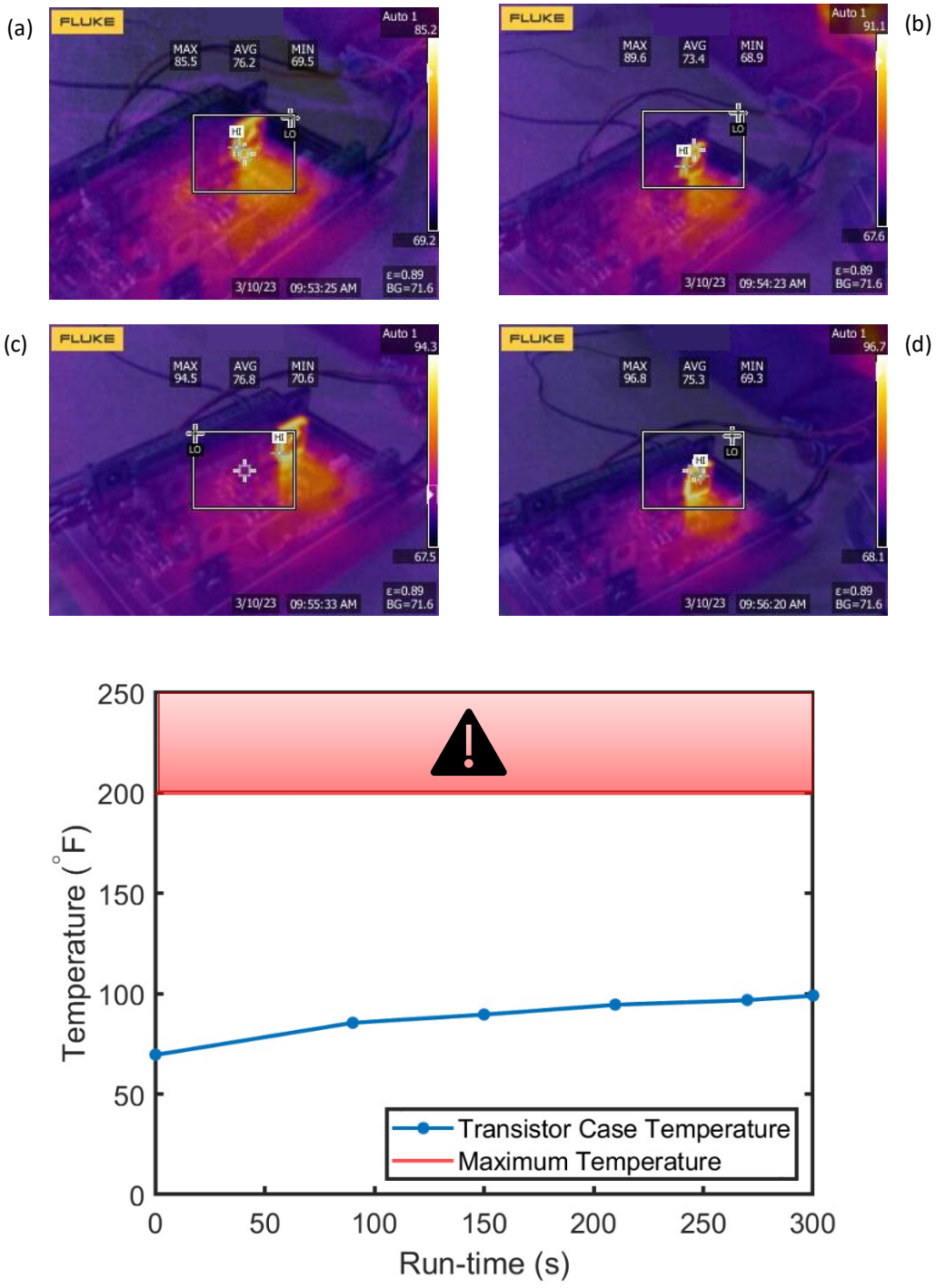

Figure A1: Thermal camera images of the automation board while supplying power to a 12-volt vacuum pump (top). Max transistor temp after 60, 90, 210, 270 seconds (a-d). Maximum case temperature plotted throughout the 5-minute run-time (bottom).

APPENDIX B

ELECTRICAL SCHEMATICS

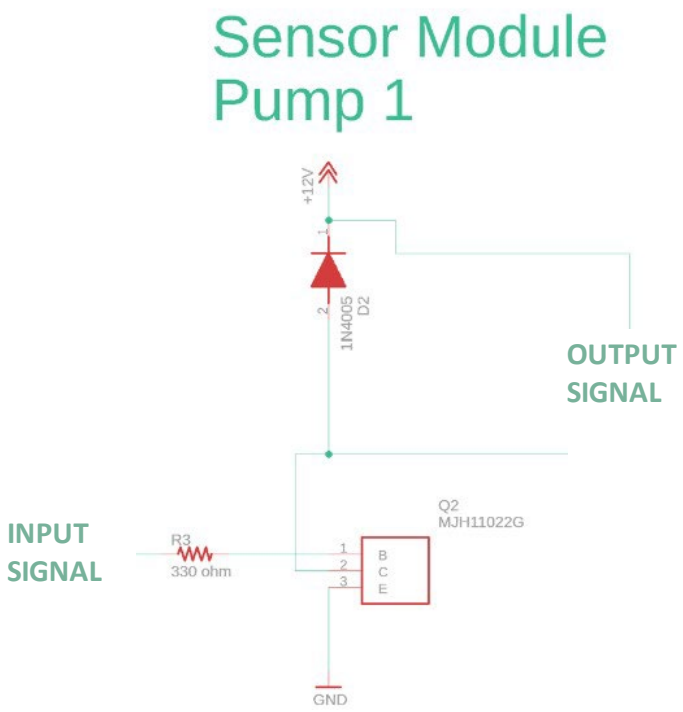

Figure B1: Control circuit used to drive vacuum pump and dispensing pumps

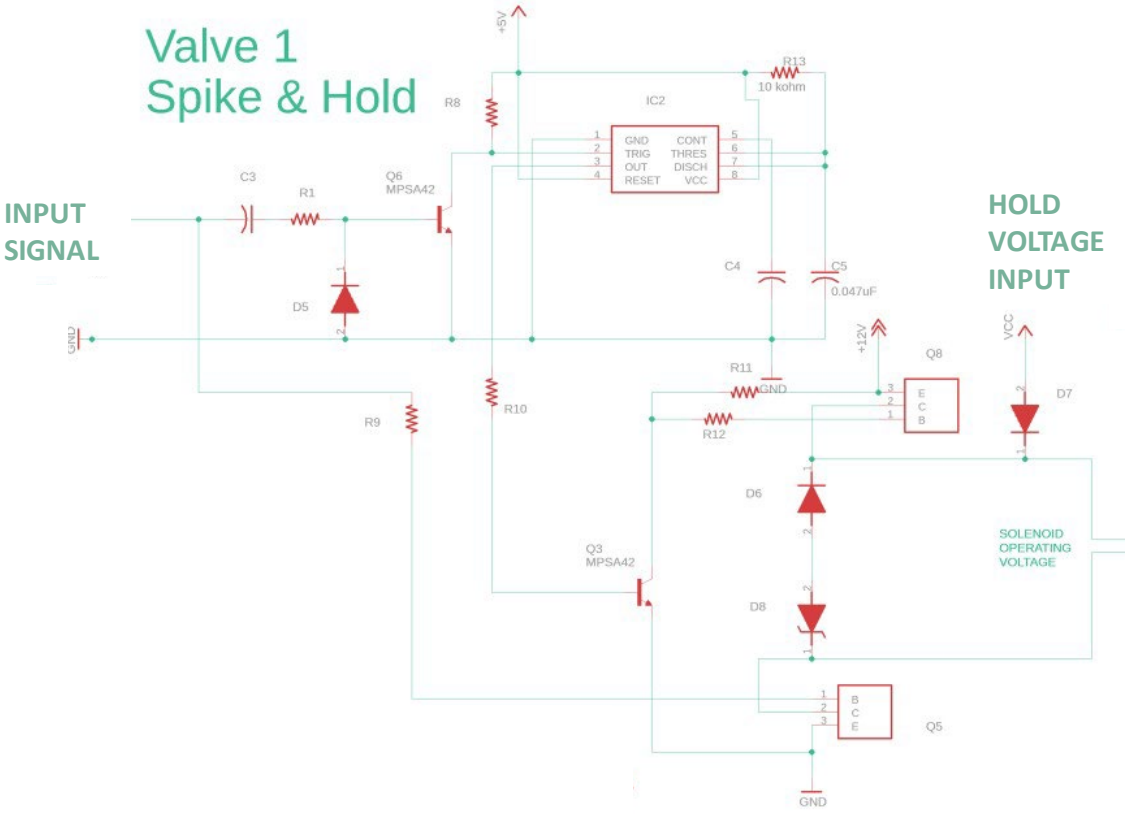

Figure B2: Control circuit used to modulate valves 1 & 2. These valves require a "Spike and Hold" signal.

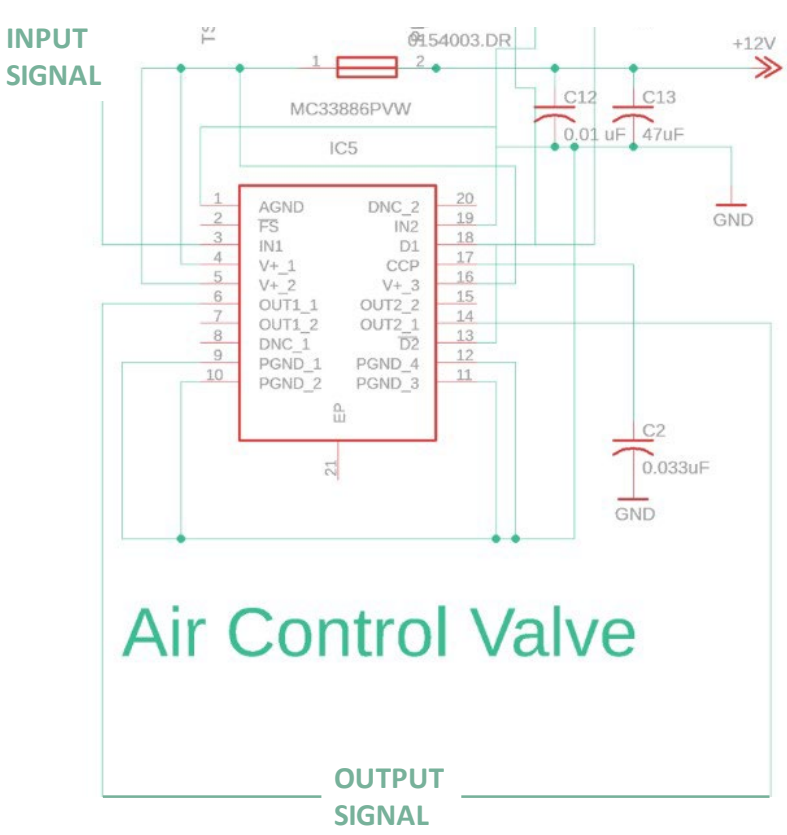

Figure B3: Control circuit to operate V3. The integrated circuit is used to supply a 12-volt polarity switching signal.

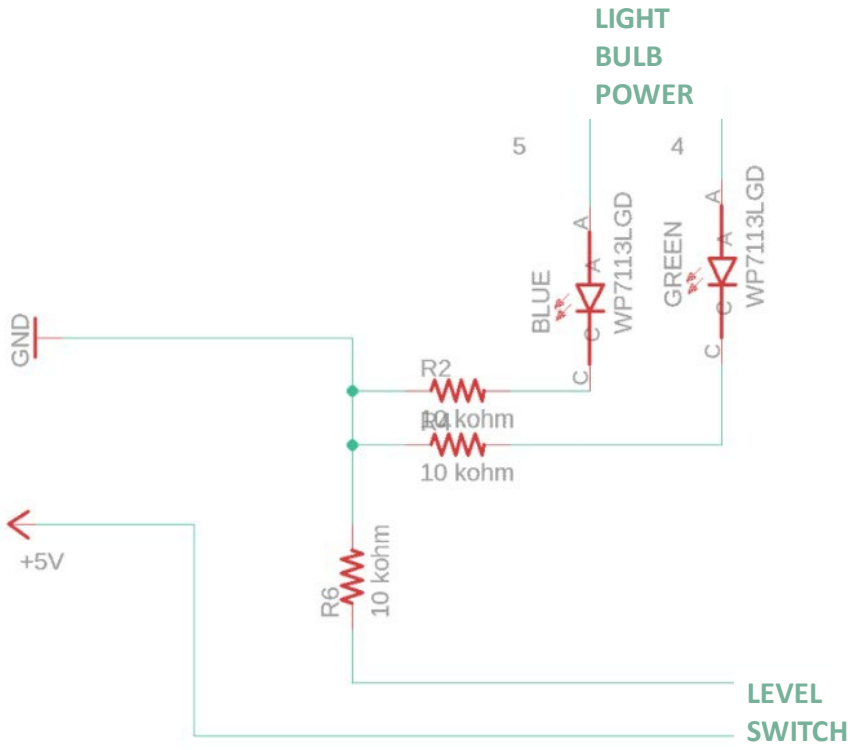

Figure B4: Level switch control circuit. The Arduino reads the analog resistance from the level switch wires to determine if the reservoir is filling or full.

APPENDIX C

LITERATURE REVIEW TABLE

Table C1:Reference used to procure the “Microsensor Technologies for Environmental Monitoring” section.

Application	**Technology**	**Transducing principle**	**Range**	**LOD**	**Advancement**	**Limitation**	**REF**
Impedance sensor for nitrate detection of soil water extracts	Electrochemical Nitrate Sensor	GO and PEDOT NFs reduce nitrate to nitrite and release an electron, this decreases the charge transfer resistance in EIS spectra	0.44 - 442 mg/l	0.135 mg/l	integrated modified electrode in microfluidic environment which has fantastic range and low limit of detection	Fig. 7d shows the transient response does not stabilize completely.	[47]
Nitrate detection in water	Optical Nitrate Sensor	A specialized sensing reflector is integrated into a fiber optical cable. At varying N concentrations, intensity peaks are shifted at measurable wavelengths	0 - 80 ppm	3 ppm	Modifying a fiber optic cable to be sensitive to N is one-of a kind. Additionally, their response time is a few milliseconds	Method requires a light source, an oscilloscope circulator and the use of a dangerous acid, HF.	[67]
Amino group modified GO solution is mixed with N and GNP	Optical Nitrate Sensor	Using UV-vis spectra, samples are mixed with a graphene oxide and amino group	0 - 0.05 uM	5 nM	Works by studying the decrease of GNP aggregation in solution	There are challenges using this in a field application.	[68]

Cu/MWCNT/ RGO Modified GCE for the sensing of nitrate and nitrite	Electrochemical Nitrate Sensor	The modified GCE shows enhanced electro-reduction of nitrite and nitrate ions in solution. Uses SWV to measure the current density responses to varying levels of Nitrate or nitrite	0.1 - 75 uM	30, 20 nM (nitrite and nitrate)	Provides an inexpensive solution to in situ monitoring of nitrate and nitrite	Great solution to use in open water but might not work as well in soils or microfluidic systems because of the probe size.	[41]
One step fab nitrate sensor using sensitive enhanced nanocomposites	Electrochemical Nitrate Sensor	Ag-rGO show excellent electrocatalytic activity in the presence of nitrate. Differential Pulse Voltammogram (DPV)	0.1 - 120 (uM)	0.012 uM	non-enzyme reduced silver graphene oxide sensor for nitrate detection	The lower bound of their range is high for N monitoring 6.2 ppm	[42]
Nitrate Ion selective electrode. Tested in tap waters	Electrochemical Nitrate Sensor	This sensor uses an ISE and an ion to electron transduction layer to drive an EMF relative to a reference electrode.	0.1 - 100 (mM)	0.01 mM	This unique sensor is a screen printed onto a flexible PET substrate. This implementation has potential	Range is not low enough for most natural water quality monitoring	[39]

Low-cost copper probe which can accurately measure EC by using EIS	Electrochemical Conductivity Sensor	EIS single frequency measurement measures the solution resistance and converts that to EC	0.5 - 20,000 (uS/cm)	0.5 uS/cm	On their board there is a range-selection mechanism which automatically activates various capacitors to enhance the range.	Size is the problem here. This probe could work great for monitoring tap water or streams but not small volumes.	[52]
Investigating the range enhancements of a 4 electrode EC sensor with IDEs	Electrochemical Conductivity Sensor	EIS single frequency measurement measures the solution resistance and converts that to EC	3 - 12,000 (uS/cm)	3 uS/cm	Microfabricated 4-electrode conductivity sensor was shown to have much better range than a 2-electrode system.	Missing an integrated sensor package. Automated systems will need this	[54]
Multifunctional pH, and EC sensor for water monitoring	Electrochemical Conductivity Sensor	ORP potential drops were used to measure pH and single frequency EIS was used for EC measurements	200 - 8000 (uS/cm)	---	Low-cost miniaturized sensor which can be used in microfluidic devices	---	[53]

LOC nitrate and Nitrite measurements of seawater	Optical Nitrate Sensor	Uses colorimetric nitrate analysis using the Griess assay. Based off of the color change when mixed with the reagent, the nitrate concentrations are determined.	0.1 - 350 uM	0.025 uM	Impressive LOC implementation of a traditional lab grade tool	Size, complexity, # of reagents that must be stored, Cadmium tube required for reduction process	[19]
A portable Optical Nitrate detection device	Optical Nitrate sensor	Uses colorimetric nitrate analysis using the Griess assay. Based off the color change when mixed with the reagent, the nitrate concentrations are determined.	1.5 - 100 uM	0.1 uM	Innovative approach to miniaturize the greiss redox process	reduced range. Still is bulky compared to electrochemical sensors	[20]
A modified gold electrode which can detect Nitrate levels using CV	Electrochemical Nitrate Sensor	Ag NPs /gold WE. The silver chemically interacts with the Nitrate and enhances the CV response	10 - 10,000 (uM)	10 uM	For the first time, an electrochemical sensor with low LOD using CV without preconcentration	Sensor requires a reference electrode.	[43]

Unique Palladium Gold modified uIDE for sensing Nitrate	Electrochemical Nitrate Sensor	The deposition of Au NP onto the surface of the IDE enhances the electro-catalytic response in LSVs	1 -15 mg/L Nitrate-N	0.074 mg/L NO3-N	Integration of an IDE into a PCB package. Clear SEM results show the formation of dendritic structures. These are extra sensitive topologies.	Requires reference electrode for CVs	[40]
Modified IDE for nitrate determination of natural waters	Electrochemical Nitrate Sensor	Ag NO3- is deposited as sensitive dendrite structures onto gold uIDE. The Ag interacts with nitrate and enhances the electrocatalytic response with SWV	2 uM	2 - 1000 uM	Microsensor for determining nitrate was developed using surface modification. Better LOD	RE required for CVs	[44]
Manufactured sensitive modified Au Microelectrodes with Ag deposition process	Electrochemical Nitrate Sensor	Ag is deposited onto an ag micro electrode array. The silver enhances the redox properties when in contact with Nitrate ions	4-1000 (uM)	3.2 uM	Extremely sensitive and reusable. Found that ammonium sulfate is required for Ag deposition	RE required for CVs	[45]

Ruthenium and Platinum modified electrodes as pH sensors	Electrochemical pH sensor	Both ruthenium and platinum have selective responses to H and OH groups. Interactions between protons in solution (hydronium) through proton exchange results in a surface potential change	5.5 - 9.0 (RuOx)	5.5 pH	Long-term performing miniaturized pH sensors with super Nernstian sensitivities	Requires RE and thin film deposition tooling	[49]
All solid-state Nitrate ISE made from nitrate doped polypyrrole	Electrochemical Nitrate sensor	Ppy (NO3) was chosen as an ISM material. Graphene here acts as an ion-to-electron transduction layer. The sensitivity was enhanced by Au NPs	10^-5 to 10^-1 M	10^-5.2 M	Enhanced sensitivity was found using the nanocomposite hybrid with gold NPs	RE required for potentiometric sensors	[35]
Nitrate sensor which uses ML training to be selective	Electrochemical Nitrate sensor	The sensor is a MWCNT IDE structure patterned on PDMS. The EIS	0.01 ppm to 30 ppm	0.01	Unique N sensor which uses software rather than material science to be selective for an	Requires large training data set, software,	[69]

		signature changes with N conc. ML and training data enhances the performance of the sensor			analyte. Cost effective	and additional hardware.	
Nitrate ISE	Electrochemical Nitrate sensor	Consist of an ISM with a PVC ion transduction layer	10^-5 - 10^-1	10^-5	All solid state, quick response time	Iodine interference was detected	[38]
Metal oxide pH sensor of a cheap and flexible substrate	Electrochemical pH sensor	ZnO and Sno2 was used as a pH sensitive material for EIS calibration	1-7 pH	1 pH	Fabricated a functional pH sensor on a miniaturized IDE structure at a low cost	basic side of the spectrum is not shown! Error bars are large	[51]
Nitrate ISE	Electrochemical Nitrate Sensor	This ISE uses a typical ISM and ion-transduction layer	8x 10^-8 - 10^-2	2.8 10^-8	This sensor uses MWCNT as the ion transducing layer because of the large double layer cap and fast charge transfer	RE required	[37]
Nitrate ISE	Electrochemical Nitrate Sensor	This ISE uses a typical ISM and ion-transduction layer	10^-5 - 10^-1 M	3.98x 10^-6 M	Introduced a new ISM material, cobalt allow/composite. Simple to manufacture	RE required	[36]

Nitrate Ion selective electrode. Direct sensing in soils	Electrochemical Nitrate Sensor	The WE have an ISM layer which only allows nitrate Ions to diffuse through the material. Then an ion to electron transduction layer drives an EMF	1.0 - 1500 ppm (NO3-N)	1.4 ppm (NO3-N)	Solid state device which works in direct contact with soil slurries and is stable over the long term. Nernstian response.	Requires nitrocellulose for fabrication of the ISM. This material is dangerous and cannot be obtained easily.	[34]
pH EIS sensor	Electrochemical pH sensor	Sensor uses RuO as a reactive metal to changes in pH, these changes enhance the interfacial behavior of the electrical double layer	3 -12 pH	pH 3	Implementation of a RuO paste using screen printing on an IDE chip	Interfering ions could be an issue, but it is not reported	[50]

APPENDIX D

SIMULATION SETUP PARAMETERS

Table D1: Simulation initial conditions parameters for COMSOL simulation study

Velocity	Pressure	Temperature	Conductivity
$0\mathbf{i} + 0\mathbf{j} + 0\mathbf{k}$ (m/s)	0 (kPa)	293.15 K	1413 ($\mu S\ cm^{-1}$)

Table D2: Simulation parameters at time = 0

Inlet Velocity	Outlet Pressure	Temperature	Inlet Conductivity
50 ($\mu l\ s^{-1}$)	0 (kPa)	293.15 K	100 ($\mu S\ cm^{-1}$)

Table D3: Boundary conditions for COMSOL simulation study

Boundary Surface	Outlet flux	Temperature	Control Volume
No slip (V = 0 m/s)	No reverse flow	293.15 K	No flux

APPENDIX E

MESA SHELL MANUFACTURING DRAWING

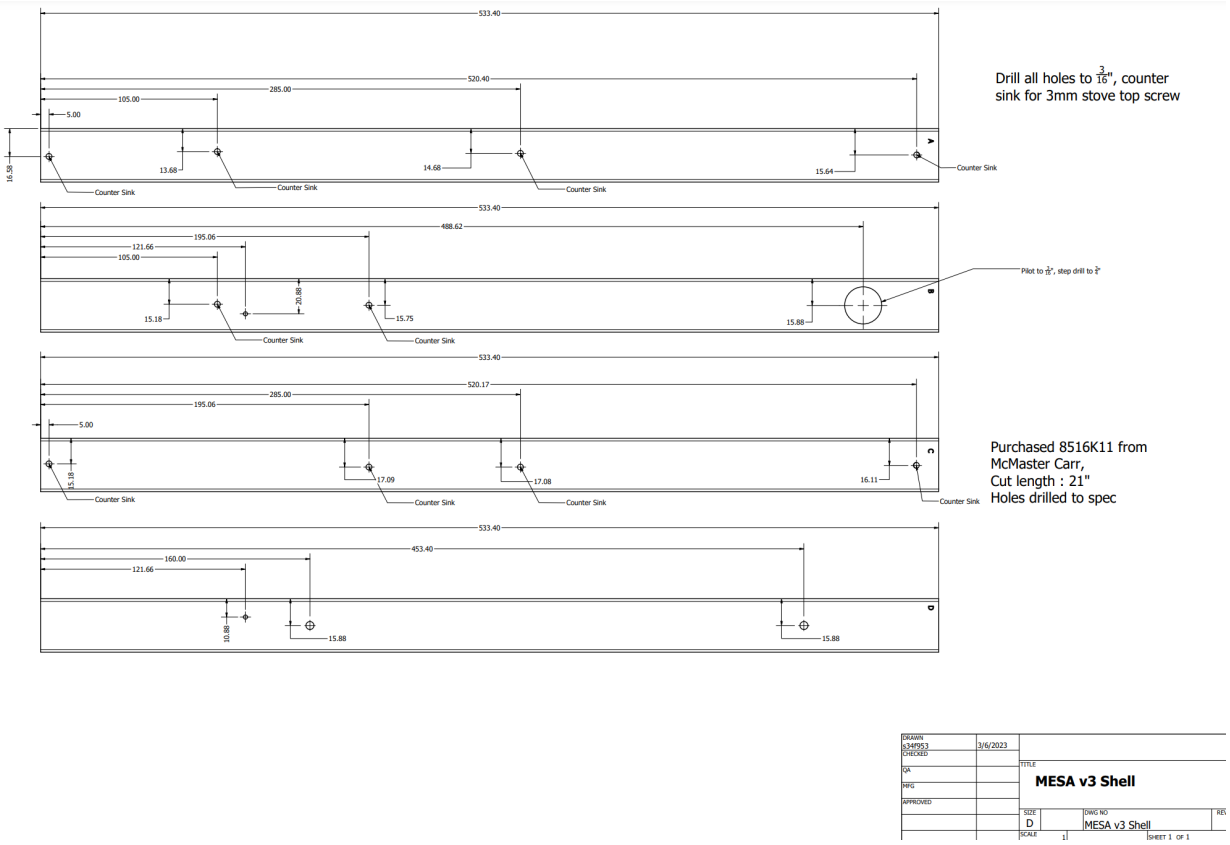

Figure E1: Manufacturing drawing for the acrylic shell. Bulk material was purchased from McMaster Carr and then modified with respect to this drawing. High quality PDF is available upon request.

APPENDIX F

AUTOMATION CONTROL BOARD LAYOUT

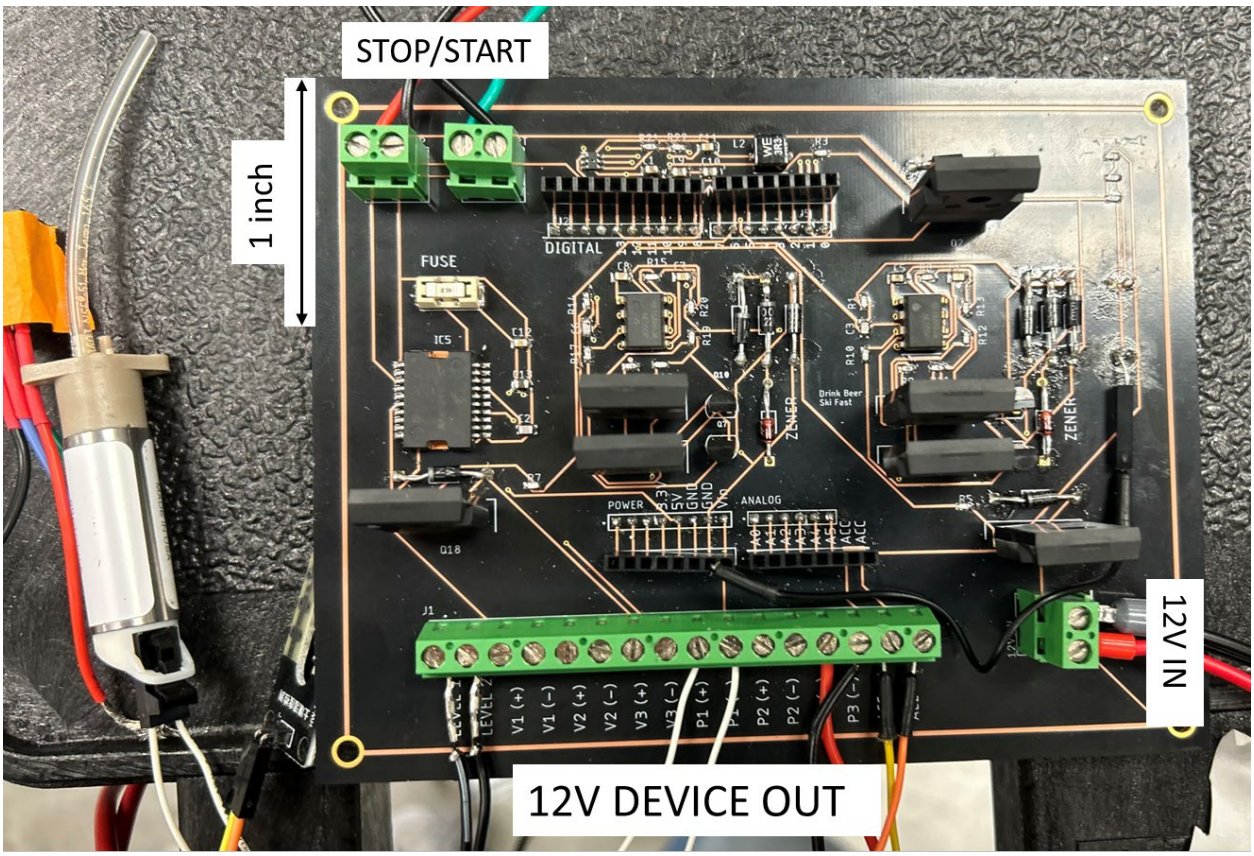

Figure F1: Automation control board layout used to control the devices shown in Figure 5. Pump one is currently connected to the board.